Strong near-infrared carbon in the Type Ia supernova iPTF13ebh[*][**]

E. Y. Hsiao[1,2], C. R. Burns[3], C. Contreras[2,1], P. Höflich[4], D. Sand[5], G. H. Marion[6,7], M. M. Phillips[2], M. Stritzinger[1],
S. González-Gaitán[8,9], R. E. Mason[10], G. Folatelli[11,12], E. Parent[13], C. Gall[1,14], R. Amanullah[15], G. C. Anupama[16],
I. Arcavi[17,18], D. P. K. Banerjee[19], Y. Beletsky[2], G. A. Blanc[3,9], J. S. Bloom[20], P. J. Brown[21], A. Campillay[2], Y. Cao[22],
A. De Cia[26], T. Diamond[4], W. L. Freedman[3], C. Gonzalez[2], A. Goobar[15], S. Holmbo[1], D. A. Howell[17,18],
J. Johansson[15], M. M. Kasliwal[3], R. P. Kirshner[7], K. Krisciunas[21], S. R. Kulkarni[22], K. Maguire[24], P. A. Milne[25],
N. Morrell[2], P. E. Nugent[23,20], E. O. Ofek[26], D. Osip[2], P. Palunas[2], D. A. Perley[22], S. E. Persson[3], A. L. Piro[3],
M. Rabus[27], M. Roth[2], J. M. Schiefelbein[21], S. Srivastav[16], M. Sullivan[28], N. B. Suntzeff[21], J. Surace[29],
P. R. Woźniak[30], and O. Yaron[26]

(Affiliations can be found after the references)

ABSTRACT

We present near-infrared (NIR) time-series spectroscopy, as well as complementary ultraviolet (UV), optical, and NIR data, of the Type Ia supernova (SN Ia) iPTF13ebh, which was discovered within two days from the estimated time of explosion. The first NIR spectrum was taken merely 2.3 days after explosion and may be the earliest NIR spectrum yet obtained of a SN Ia. The most striking features in the spectrum are several NIR C I lines, and the C I $\lambda1.0693$ μm line is the strongest ever observed in a SN Ia. Interestingly, no strong optical C II counterparts were found, even though the optical spectroscopic time series began early and is densely cadenced. Except at the very early epochs, within a few days from the time of explosion, we show that the strong NIR C I compared to the weaker optical C II appears to be general in SNe Ia. iPTF13ebh is a fast decliner with $\Delta m_{15}(B) = 1.79 \pm 0.01$, and its absolute magnitude obeys the linear part of the width-luminosity relation. It is therefore categorized as a "transitional" event, on the fast-declining end of normal SNe Ia as opposed to subluminous/91bg-like objects. iPTF13ebh shows NIR spectroscopic properties that are distinct from both the normal and subluminous/91bg-like classes, bridging the observed characteristics of the two classes. These NIR observations suggest that composition and density of the inner core are similar to that of 91bg-like events, and that it has a deep-reaching carbon burning layer that is not observed in more slowly declining SNe Ia. There is also a substantial difference between the explosion times inferred from the early-time light curve and the velocity evolution of the Si II $\lambda0.6355$ μm line, implying a long dark phase of ~4 days.

Key words. infrared: general – supernovae: general – supernovae: individual: iPTF13ebh

1. Introduction

Type Ia supernovae (SNe Ia), with empirically calibrated luminosities, provide a direct measure of the expansion history of the universe and led to the discovery of the accelerated expansion (Riess et al. 1998; Perlmutter et al. 1999). The goal of reaching the 1−2% distance precision (Albrecht et al. 2006) or $\sigma_w \approx 2\sigma_m$ (Goobar & Leibundgut 2011) for the next-generation SN Ia experiments critically depends on minimizing the systematic errors in the distance determinations. One of the most important open questions is the potential evolution of the empirical calibration with redshift. Given the wide range of look-back time considered, such an evolution could be caused by changes in the mean host metallicity and stellar mass with redshift (e.g., Sullivan et al. 2010). A deeper understanding of the physics of SNe Ia could help to estimate this systematic error and perhaps even mitigate its effects.

It is general consensus that the origin of a SN Ia is the thermonuclear explosion of a carbon-oxygen white dwarf (Hoyle & Fowler 1960). Since oxygen is also produced from carbon burning, carbon provides the most direct probe of the primordial material from the progenitor. The quantity, distribution, and incidence of unburned carbon in SNe Ia provide important constraints for explosion models. Turbulent deflagration models predict that a large amount of unprocessed carbon remains (Gamezo et al. 2003; Röpke et al. 2007). Three-dimensional simulations of pure deflagrations predict a significant amount of unburned material in the inner ejecta, which contradicts observations (e.g., Kozma et al. 2005). In one-dimensional simulations, a transition to a detonation is expected to result in complete carbon burning (Höflich et al. 2002; Marion et al. 2006; Kasen et al. 2009), although there are exceptions. Three-dimensional effects in delayed-detonation models can create pockets of unburned material in the ejecta (Gamezo et al. 2004). In the case of pulsating delayed-detonation models (PDD; Höflich et al. 1996), the initial pulsation allows the outer ejecta to become loosely bound. The low density of this material subsequently quenches the nuclear burning. This leaves more unburned carbon than in standard delayed-detonation models (Dessart et al. 2014).

The identification of the weak absorption feature near 0.63 μm in the normal SN Ia SN 1998aq as C II λ0.6580 μm was first suggested by Branch et al. (2003). Garavini et al. (2004) then noted possible contributions of C II and C III in SN 1999aa. Thomas et al. (2007) presented convincing detections of the C II $\lambda\lambda$0.4267, 0.6580, and 0.7234 lines in the early optical spectra of SN 2006D. C II λ0.6580 μm has also been detected in the luminous and slowly expanding super-Chandrasekhar candidates: strong C II lines in SN 2009dc (Silverman et al. 2011; Taubenberger et al. 2011), and marginal detections in SN 2003fg (Howell et al. 2006) and SN 2007if (Scalzo et al. 2010). In subsequent studies with larger optical spectroscopic samples, 20−30% of the pre-maximum spectra were found to show C II signatures (Thomas et al. 2011a; Parrent et al. 2011; Folatelli et al. 2012; Silverman & Filippenko 2012). Several of these studies noted, however, that this fraction represents a lower limit because noise, line overlap, and the phase at which the SNe Ia were observed could affect the C II detection (e.g., Branch et al. 2007; Folatelli et al. 2012).

The velocities of the detected C II lines are generally low. There have also been hints that SNe Ia with detected C II have preferentially bluer colors and narrower light curves (Thomas et al. 2011a; Folatelli et al. 2012; Silverman & Filippenko 2012; Maguire et al. 2014), but this preference was not clear in the examinations of other data sets (e.g., Parrent et al. 2011; Blondin et al. 2012). Milne et al. (2013) also noted a strong preference for blue ultraviolet (UV) colors in SNe Ia with carbon detections. There appears to be a consensus that the mass fraction of carbon is low (e.g., Branch et al. 2003; Marion et al. 2006; Thomas et al. 2007; Tanaka et al. 2008). SNe Ia that display signatures of carbon tend to have lower Si II velocities, while the objects without carbon span the entire range of Si II velocities (e.g., Folatelli et al. 2012; Silverman & Filippenko 2012). This phenomenon may be an observational bias as the C II λ0.6580 μm at high velocities is shifted into the prominent Si II λ0.6355 μm line. It could also be a physical bias. The PDD models of Dessart et al. (2014) predict both strong carbon lines and relatively narrow Si II λ0.6355 μm absorption, while their standard delayed-detonation models predict no carbon and broad Si II lines. Several characteristics of unburned material established by the optical C II lines may be uncertain because of the observational challenges posed by capturing an unbiased sample of these features.

Near-infrared (NIR) spectroscopy of SNe Ia has been shown to provide links between observables and explosion physics (e.g., Wheeler et al. 1998; Höflich et al. 2004; Motohara et al. 2006; Friesen et al. 2014; Diamond et al. 2014). Marion et al. (2006) pioneered the study of NIR carbon features. Examining the C I lines in NIR spectra of three normal SNe Ia, they concluded that the abundance of unprocessed material is low. The early discovery of the nearby SN 2011fe offered an unprecedented opportunity to study the NIR carbon features in detail. With the aid of NIR spectra with a high signal-to-noise ratio and the automated spectrum synthesis code SYNAPPS (Thomas et al. 2011b), Hsiao et al. (2013) inferred the presence of the C I λ1.0693 μm line in SN 2011fe from the flattening of the emission component of the Mg II λ1.0092 μm P-Cygni profile. The NIR C I line has the same velocity as the optical C II λ0.6580 μm line and increases in strength toward maximum light, in contrast to the fast-fading nature of the optical C II line. Hsiao et al. (2013) suggested that this delayed onset of the NIR C I line is an ionization effect and pointed out its potential to secure more representative properties of unburned material in SNe Ia.

iPTF13ebh is a SN Ia discovered at an exceptionally young age by the intermediate Palomar Transient Factory (iPTF). The first NIR spectrum was taken merely 2.3 days past the explosion, allowing the examination of material in the outermost ejecta. Strong NIR C I λ1.0693 μm is present in the first two NIR spectra. To our knowledge, this marks the fourth detection of NIR C I so far in a SN Ia, along with SNe 1999by (Höflich et al. 2002), 2011fe (Hsiao et al. 2013), and 2014J (Marion et al. 2015). In fact, the C I feature of iPTF13ebh is the strongest ever observed. As the supernova evolved, it became clear that the time evolution of the NIR C I feature was very different from that of any other previous detection, and that iPTF13ebh had fast-declining light curves. Examination of the optical spectra showed no apparent Ti II feature that would qualify it as a 91bg-like object (Filippenko et al. 1992). The NIR primary maxima also occurred before the B maximum. This places iPTF13ebh in the class of "transitional" objects, whose notable members include SNe 1986G (Phillips et al. 1987), 2003gs (Krisciunas et al. 2009), 2004eo (Pastorello et al. 2007; Mazzali et al. 2008), 2009an (Sahu et al. 2013), 2011iv (Foley et al. 2012), and 2012ht (Yamanaka et al. 2014). In this paper, we focus on examining the NIR spectroscopic properties of iPTF13ebh and highlight how they differ from those of normal and 91bg-like objects. These differences could shed light on the connections between normal and 91bg-like objects.

2. Observations and reduction

iPTF13ebh was discovered in NGC 890 by iPTF in an image taken with the Palomar 48-inch telescope (P48; Rahmer et al. 2008) on 2013 November 13.15 UT (Cao et al. 2013). Within hours of the discovery, the Carnegie Supernova Project (CSP) obtained a NIR spectrum with the Folded-port Infrared Echellette (FIRE; Simcoe et al. 2013) mounted on the *Magellan Baade* Telescope on 2013 November 14.16 UT. Using a quick reduction pipeline based on the `firehose` package[1], a spectrum was produced from the first two frames within 10 min of acquiring the target. The supernova was classified as a young SN Ia with several strong features produced by intermediate-mass elements (Cao et al. 2013). More frames were subsequently obtained to reach the desired signal-to-noise ratio. An optical spectrum taken on 2013 November 15.83 UT later confirmed the NIR classification (Maguire et al. 2013). Reprocessing of the P48 images from preceding nights showed that the supernova was visible on an image taken on 2013 November 12.21, at 20.9 ± 0.2 mag, and not detected in an image taken 2013 November 11.25 UT down to 21.7 mag. Intense follow-up of iPTF13ebh was conducted in the optical and NIR as part of the CSP, in collaboration with iPTF and the CfA Supernova Group.

2.1. Photometric observations

The discovery and a small number of follow-up images were taken with the P48 in the *r*-band. Host galaxy subtractions were performed using a deep reference of NGC 890 constructed from images taken before the explosion. The point-spread function (PSF) was determined and matched before each subtraction and was subsequently used for PSF photometry on the subtracted frames. The P48 photometry is presented in Table 1.

Swope follow-up in *uBVgri* began on the same night that the FIRE classification spectrum was obtained. All images were taken with the newly commissioned e2v CCD imager, which is more efficient overall and specifically more sensitive in the blue than the previous CCD employed by the CSP. The pixel size of

---

[1] Available at http://web.mit.edu/~rsimcoe/www/FIRE/

Table 1. Journal of the P48 photometric observations.

MJD	r
56 608.21	20.94 (0.21)
56 609.15	18.89 (0.06)
56 623.09	15.14 (0.01)
56 624.08	15.15 (0.01)
56 625.26	15.15 (0.01)
56 626.14	15.16 (0.01)
56 648.09	16.60 (0.01)

Notes. The MJD column lists the Modified Julian Date of each observation. The P48 photometry is host galaxy subtracted.
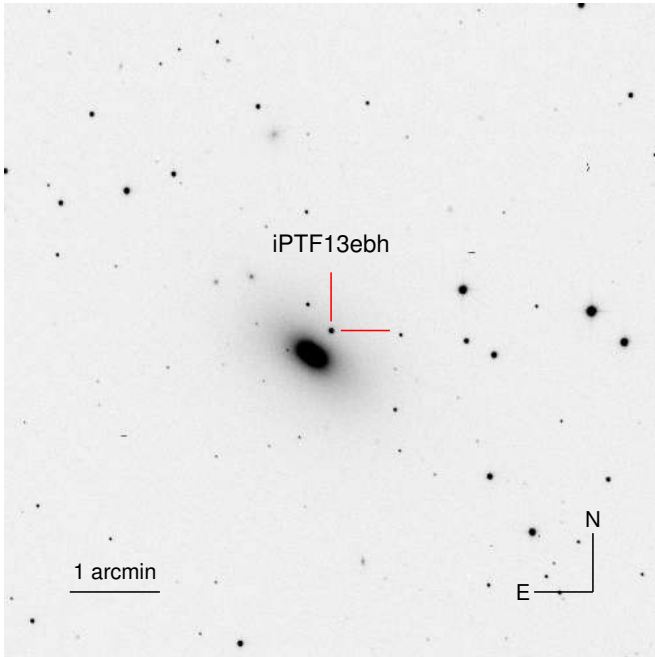

Fig. 1. Swope r-band image of iPTF13ebh in NGC 890 taken near maximum light. The cross hair marks the location of the supernova. The compass and the size of the field are also noted.

0.′′435 remains the same. The 2×2 CCD array yields a field of view of approximately 30′ on each side. The supernova and standard fields are normally placed at the center of one pre-selected quadrant. The bandpass functions with the new e2v imager have been characterized with a spectrometer in the same manner as described in Rheault et al. (2010) and Stritzinger et al. (2011). The results are presented in Rheault et al. (2014). A Swope r-band image taken near maximum light is shown in Fig. 1. The Swope images were reduced as described in Contreras et al. (2010). PSF photometry was performed with respect to a local sequence of standard stars calibrated to the Landolt (1992) and Smith et al. (2002) standard fields. The standard fields were observed on the same nights as the supernova observations over the course of 20 photometric nights. The Swope photometry is tabulated in Table 2.

The light curves obtained with Swope and P48 are presented in the standard Landolt (1992) and Smith et al. (2002) systems in Fig. 2. Note that the Swope light curves are without host galaxy template subtractions, and no host galaxy or Milky Way dust extinction corrections have been applied. From Fig. 1, the site of iPTF13ebh does not appear to be substantially host galaxy contaminated. Hence, the unsubtracted photometry should be adequate for determining basic photometric parameters. This is
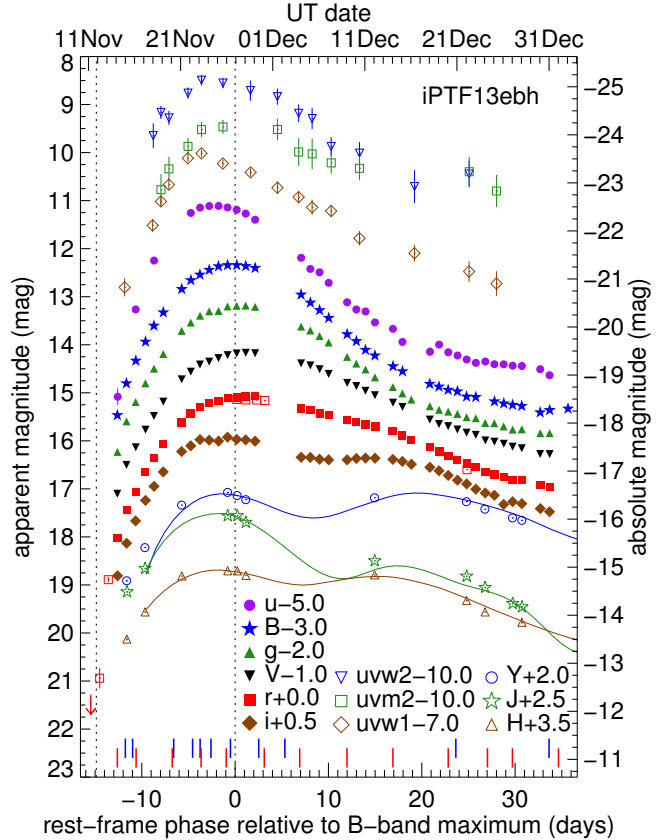

Fig. 2. UV, optical, and NIR light curves of iPTF13ebh. The *uvw*2, *uvm*2, and *uvw*1 light curves are obtained with UVOT on *Swift*; the *uBVgri* light curves are obtained with the e2v imager on Swope; and the *YJH* light curves are obtained with RetroCam on *du Pont*. All of these are without host subtractions. For the r-band light curve, open red square symbols represent host-subtracted r-band data from P48. A downward arrow marks the date of a non-detection image from P48 down to a magnitude limit of 21.7 mag. SNooPy fits (Burns et al. 2011) are plotted for the more sparsely sampled NIR light curves. Blue and red vertical dash lines mark the dates when the optical and NIR spectra are taken, respectively. Two black vertical dotted lines are drawn at the inferred time of explosion and time of B-band maximum. The absolute magnitude is computed using a distance modulus of 33.63, derived from the host recession velocity of Woods et al. (2006).

corroborated by the comparison of the Swope and P48 r-band light curves. On nights when both Swope and P48 r-band photometry is available, the Swope points are consistently brighter, but by only ∼0.01 mag on average.

The NIR *YJH* light curves were obtained using RetroCam, which was moved from the 1 m Swope to the 2.5 m *du Pont* telescope in 2011. The single-chip Rockwell HAWAII-1 HgCdTe detector and 0.′′201 pixel size yield a field of view of 3.′5 on each side. The images were reduced in the standard manner following Contreras et al. (2010). As in the optical, the NIR photometry was computed differentially with respect to a local sequence of stars. The local sequence was then calibrated to the Persson et al. (1998) system in the *JH*-bands, with the standard fields observed during six photometric nights. The *Y*-band was calibrated to a set of not yet published magnitudes of the Persson standards. The NIR light curves are also without host galaxy template subtractions. The RetroCam photometry is tabulated in Table 3.

We also present UV *uvw*1, *uvm*2, and *uvw*2 light curves obtained with the UltraViolet Optical Telescope (UVOT; Roming et al. 2005) on the *Swift* Mission (Gehrels et al. 2004).

Table 2. Journal of the Swope e2v photometric observations.

MJD	B	V	u	g	r	i
56 610.13	18.466 (0.024)	18.101 (0.021)	20.082 (0.172)	18.230 (0.017)	18.027 (0.020)	18.309 (0.046)
56 611.12	17.803 (0.020)	17.501 (0.015)	$\cdots$	17.595 (0.013)	17.435 (0.018)	17.632 (0.029)
56 612.14	17.332 (0.014)	17.134 (0.014)	18.265 (0.063)	17.193 (0.013)	17.056 (0.012)	17.166 (0.019)
56 613.19	16.937 (0.019)	16.768 (0.013)	$\cdots$	16.803 (0.011)	16.654 (0.011)	16.740 (0.013)
56 614.10	16.604 (0.009)	16.482 (0.008)	17.247 (0.023)	16.497 (0.008)	16.362 (0.007)	16.447 (0.011)
56 615.13	16.327 (0.009)	16.184 (0.007)	$\cdots$	16.192 (0.006)	16.057 (0.006)	16.147 (0.008)
56 617.12	15.841 (0.006)	15.720 (0.007)	$\cdots$	15.711 (0.006)	15.609 (0.008)	15.722 (0.016)
56 618.12	15.656 (0.005)	15.560 (0.006)	16.256 (0.009)	15.539 (0.005)	15.441 (0.006)	15.603 (0.007)
56 619.10	15.541 (0.006)	15.411 (0.009)	16.145 (0.009)	15.395 (0.008)	15.288 (0.009)	15.474 (0.013)
56 620.11	15.442 (0.007)	15.352 (0.008)	16.112 (0.012)	15.304 (0.007)	15.210 (0.012)	15.486 (0.012)
56 621.11	15.368 (0.007)	15.278 (0.006)	16.111 (0.029)	15.296 (0.006)	15.168 (0.006)	15.505 (0.018)
56 622.10	15.343 (0.005)	15.216 (0.005)	16.142 (0.009)	15.202 (0.005)	15.109 (0.006)	15.423 (0.007)
56 623.09	15.343 (0.006)	15.181 (0.008)	16.191 (0.011)	15.189 (0.005)	15.099 (0.009)	15.469 (0.011)
56 624.07	15.361 (0.007)	15.167 (0.006)	16.270 (0.013)	15.185 (0.005)	15.068 (0.006)	15.480 (0.010)
56 625.09	15.401 (0.006)	15.176 (0.006)	16.397 (0.014)	15.211 (0.005)	15.059 (0.007)	15.507 (0.009)
56 630.08	15.956 (0.011)	15.388 (0.012)	17.190 (0.026)	15.622 (0.010)	15.322 (0.012)	15.841 (0.016)
56 631.09	16.124 (0.007)	15.430 (0.006)	17.421 (0.021)	15.703 (0.006)	15.360 (0.007)	15.846 (0.013)
56 632.09	16.280 (0.008)	15.509 (0.007)	17.492 (0.015)	15.818 (0.005)	15.430 (0.008)	15.883 (0.011)
56 633.08	16.442 (0.011)	15.607 (0.008)	17.711 (0.018)	15.953 (0.009)	15.462 (0.010)	15.895 (0.013)
56 635.08	16.781 (0.014)	15.794 (0.007)	18.116 (0.030)	16.252 (0.006)	15.558 (0.006)	15.895 (0.009)
56 636.08	16.925 (0.014)	15.860 (0.009)	18.266 (0.036)	16.392 (0.008)	15.612 (0.009)	15.867 (0.013)
56 637.07	17.107 (0.021)	15.958 (0.008)	18.307 (0.047)	16.514 (0.008)	15.653 (0.006)	15.859 (0.008)
56 638.10	17.224 (0.017)	16.050 (0.008)	18.535 (0.034)	16.678 (0.010)	15.693 (0.008)	15.862 (0.011)
56 640.06	17.447 (0.023)	16.206 (0.014)	18.668 (0.047)	16.880 (0.012)	15.804 (0.008)	15.886 (0.009)
56 641.09	17.553 (0.031)	16.295 (0.011)	18.941 (0.084)	17.012 (0.015)	15.890 (0.007)	15.928 (0.009)
56 644.05	17.815 (0.026)	16.557 (0.011)	19.145 (0.092)	17.279 (0.019)	16.131 (0.008)	16.050 (0.010)
56 645.05	17.872 (0.019)	16.650 (0.010)	18.997 (0.050)	17.354 (0.014)	16.232 (0.008)	16.123 (0.013)
56 646.05	17.939 (0.013)	16.694 (0.010)	19.157 (0.030)	17.392 (0.013)	16.317 (0.011)	16.220 (0.013)
56 647.05	17.971 (0.014)	16.764 (0.012)	19.224 (0.029)	17.440 (0.012)	16.399 (0.011)	16.318 (0.013)
56 648.05	18.079 (0.015)	16.830 (0.010)	19.307 (0.035)	17.507 (0.014)	16.473 (0.011)	16.397 (0.014)
56 649.05	18.089 (0.015)	16.876 (0.011)	19.376 (0.039)	17.529 (0.012)	16.539 (0.012)	16.506 (0.014)
56 651.07	18.179 (0.018)	17.017 (0.013)	19.405 (0.038)	17.634 (0.014)	16.694 (0.013)	16.634 (0.018)
56 652.09	18.222 (0.023)	17.061 (0.013)	19.407 (0.068)	17.700 (0.015)	16.760 (0.017)	16.824 (0.026)
56 653.04	18.251 (0.017)	17.121 (0.013)	19.436 (0.028)	17.765 (0.017)	16.818 (0.017)	16.767 (0.023)
56 654.04	18.274 (0.020)	17.154 (0.012)	19.442 (0.031)	17.761 (0.013)	16.824 (0.012)	16.808 (0.018)
56 656.04	18.408 (0.027)	17.273 (0.020)	19.509 (0.053)	17.842 (0.016)	16.913 (0.014)	16.911 (0.019)
56 657.07	18.360 (0.016)	17.276 (0.015)	19.634 (0.041)	17.840 (0.015)	16.971 (0.015)	16.976 (0.016)
56 659.06	18.330 (0.018)	$\cdots$	$\cdots$	$\cdots$	$\cdots$	$\cdots$

Notes. The MJD column lists the Modified Julian Date of each observation. The Swope photometry is without host subtraction.

Table 3. Journal of the *du Pont* RetroCam photometric observations.

MJD	Y	J	H
56 611.14	16.913 (0.016)	16.643 (0.022)	16.627 (0.028)
56 613.12	16.223 (0.011)	16.156 (0.014)	16.063 (0.016)
56 617.11	15.338 (0.009)	$\cdots$	15.315 (0.011)
56 622.10	15.073 (0.009)	15.059 (0.009)	15.206 (0.011)
56 623.14	15.139 (0.009)	15.058 (0.009)	15.207 (0.013)
56 624.07	15.225 (0.009)	15.196 (0.009)	15.303 (0.011)
56 638.05	15.186 (0.009)	15.996 (0.012)	15.291 (0.012)
56 648.03	15.267 (0.009)	16.317 (0.014)	15.824 (0.022)
56 650.04	15.422 (0.009)	16.552 (0.019)	16.063 (0.020)
56 653.03	15.605 (0.010)	16.884 (0.023)	$\cdots$
56 654.04	15.655 (0.011)	16.956 (0.028)	16.277 (0.035)

Notes. The MJD column lists the Modified Julian Date of each observation. The RetroCam photometry is without host subtraction.

The photometry follows the method outlined by Brown et al. (2012, 2014a), which incorporates the updated zero points and time-dependent sensitivity corrections of Breeveld et al. (2011). Note that host galaxy templates are not yet available to remove the non-SN counts. The UVOT photometry is tabulated in Table 4.

Table 4. Journal of the *Swift* UVOT photometric observations.

MJD	$uvw2$	$uvm2$	$uvw1$
56 610.9	$\cdots$	$\cdots$	19.805 (0.187)
566 14.0	19.647 (0.256)	$\cdots$	18.515 (0.133)
56 614.9	19.162 (0.136)	20.773 (0.326)	18.017 (0.101)
56 615.7	19.277 (0.147)	20.339 (0.250)	17.667 (0.092)
56 617.8	18.761 (0.116)	19.870 (0.181)	17.117 (0.077)
56 619.3	18.492 (0.110)	19.522 (0.159)	17.016 (0.077)
56 621.6	18.551 (0.108)	19.465 (0.146)	17.228 (0.079)
56 624.6	18.708 (0.212)	$\cdots$	17.411 (0.083)
56 627.5	18.835 (0.169)	19.520 (0.225)	17.731 (0.126)
56 629.8	19.181 (0.185)	19.987 (0.290)	17.927 (0.130)
56 631.3	19.291 (0.219)	20.027 (0.321)	18.138 (0.158)
56 633.3	19.872 (0.194)	20.214 (0.226)	18.215 (0.110)
56 636.4	20.009 (0.228)	20.327 (0.249)	18.785 (0.149)
56 642.4	20.706 (0.341)	$\cdots$	19.094 (0.172)
56 648.3	20.445 (0.277)	20.398 (0.309)	19.475 (0.215)
56 651.3	$\cdots$	20.800 (0.334)	19.726 (0.256)

Notes. The MJD column lists the Modified Julian Date of each observation. The UVOT photometry is without host subtraction.

Table 5. Journal of optical spectroscopic observations.

UT Date	MJD	Instrument	$t_{max}(B)$	t_{exp}
2013-11-15	56 611.00	WHT + ISIS	−11.9	3.2
2013-11-16	56 611.79	HCT + HFOSC	−11.1	3.9
2013-11-20	56 616.25	ARC + DIS	−6.7	8.4
2013-11-22	56 618.30	FTN + FLOYDS	−4.6	10.4
2013-11-23	56 619.12	NOT + ALFOSC	−3.8	11.3
2013-11-24	56 620.30	FTN + FLOYDS	−2.6	12.5
2013-11-26	56 622.41	P200 + DBSP	−0.5	14.6
2013-11-29	56 625.48	Keck + DEIMOS	+2.6	17.6
2013-12-02	56 628.32	Keck + LRIS	+5.4	20.5
2013-12-20	56 646.88	NOT + ALFOSC	+24.0	39.0
2013-12-31	56 657.00	*Magellan* + IMACS	+34.1	49.2

Notes. The MJD column lists the Modified Julian Date of each observation. We adopt the time of B maximum of JD 2 456 623.4 and the time of explosion of JD 2 456 608.4 for the phase relative to B-band maximum, $t_{max}(B)$, and phase relative to explosion, t_{exp}, respectively.

2.2. Spectroscopic observations

Through the iPTF collaboration, low-resolution optical spectra were obtained from a variety of instruments. These include the Intermediate dispersion Spectrograph and Imaging System (ISIS) on the *William Herschel* Telescope (WHT), the Himalaya Faint Object Spectrograph Camera (HFOSC) on the Himalayan *Chandra* Telescope (HCT), the Dual Imaging Spectrograph (DIS) on the ARC 3.5 m telescope, the cross-dispersed spectrograph FLOYDS on the robotic Faulkes Telescope North (FTN), the Andalucia Faint Object Spectrograph and Camera (ALFOSC) on the Nordic Optical Telescope (NOT), the Double Beam Spectrograph (DBSP; Oke & Gunn 1982) on the Palomar 200-inch telescope (P200), the Deep Imaging Multi-Object Spectrograph (DEIMOS; Faber et al. 2003) on the Keck II telescope, the Low Resolution Imaging Spectrometer (LRIS; Oke et al. 1995) on the Keck I telescope, and the Inamori *Magellan* Areal Camera and Spectrograph (IMACS; Dressler et al. 2011) on the *Magellan* Telescope. A journal of observations is presented in Table 5 and the spectra are plotted in Fig. 3. The spectra are made public via the WISeREP database (Yaron & Gal-Yam 2012).

The NIR spectroscopic time series of iPTF13ebh was obtained using FIRE (Simcoe et al. 2013) on the *Magellan* Telescope, GNIRS (Elias et al. 1998) on the Gemini North Telescope, and SpeX (Rayner et al. 2003) on the NASA Infrared Telescope Facility (IRTF) as part of a joint CSP-CfA Supernova Group program to obtain time-series NIR spectroscopy of supernovae. The combination of classically scheduled time on *Magellan* and target-of-opportunity queue observing on Gemini North allowed spectra to be obtained in a regular 2–4 day cadence when the supernova was young. The observing log is presented in Table 6. The NIR spectroscopic time series is presented in Fig. 4.

The FIRE spectra were obtained in the high-throughput prism mode with a 0″6 slit. This configuration yields a continuous wavelength coverage from 0.8 to 2.5 μm with a resolution of $R \sim 500$ in the J-band. When acquiring the supernova, the slit was oriented along the parallactic angle to minimize the effect of differential refraction (Filippenko 1982). At each epoch, several frames were obtained using the conventional ABBA nod-along-the-slit technique and the sampling-up-the-ramp readout mode. The per-frame exposure time was between 95.1 and 158.5 s depending on the brightness of the supernova. These exposure

Table 6. Journal of the NIR spectroscopic observations.

UT Date	MJD	Instrument	$t_{max}(B)$	t_{exp}	T_{int}
2013-11-14	56 610.14	FIRE	−12.8 d	2.3 d	52.8
2013-11-16	56 612.17	FIRE	−10.7 d	4.3 d	21.1
2013-11-20	56 616.10	FIRE	−6.8 d	8.2 d	25.4
2013-11-23	56 619.23	GNIRS	−3.7 d	11.4 d	40.0
2013-11-26	56 621.96	GNIRS	−1.0 d	14.1 d	32.0
2013-11-30	56 626.08	FIRE	+3.2 d	18.2 d	19.0
2013-12-04	56 630.43	GNIRS	+7.4 d	22.7 d	30.0
2013-12-09	56 635.06	FIRE	+12.1 d	27.2 d	25.4
2013-12-14	56 640.05	FIRE	+17.1 d	32.2 d	16.9
2013-12-20	56 646.05	FIRE	+23.1 d	38.2 d	16.9
2013-12-24	56 650.32	SpeX	+27.4 d	42.5 d	30.0
2013-12-27	56 653.03	FIRE	+30.1 d	45.2 d	16.9
2014-01-01	56 658.03	FIRE	+35.1 d	50.2 d	16.9

Notes. The MJD column lists the Modified Julian Date of each observation. We adopt the time of B maximum of JD 2 456 623.4 and the time of explosion of JD 2 456 608.4 for the phase relative to B-band maximum, $t_{max}(B)$, and phase relative to explosion, t_{exp}, respectively. T_{int} represents the total on-target integration time in minutes.

times were chosen such that an adequate signal was obtained in each frame without saturating the bright sky lines in the K-band. At each epoch, an A0V star was observed close to the science observations in time, angular distance and air mass for telluric correction, following the method described in Vacca et al. (2003).

The data were reduced using the IDL pipeline `firehose`, which is specifically designed to reduce FIRE data. The pipeline performed steps of flat fielding, wavelength calibration, sky subtraction, spectral tracing, and extraction. The sky flux was modeled using off-source pixels as described by Kelson (2003) and was subtracted from each frame. The spectral extraction was then performed using the optimal technique (Horne 1986), a weighting scheme that delivers the maximum signal-to-noise ratio while preserving spectrophotometric accuracy. Individual spectra were then combined with sigma clipping to reject spurious pixels. Corrections for telluric absorption were performed using the IDL tool `xtellcor` developed by Vacca et al. (2003). To construct a telluric correction spectrum free of stellar absorption features, a model spectrum of Vega was used to match and remove the hydrogen lines of the Paschen and Brackett series from the A0V telluric standard. The resulting telluric correction spectrum was also used for flux calibration.

The GNIRS spectra were observed in the cross-dispersed mode in combination with the short-wavelength camera, a 32 lines per mm grating, and 0″675 slit. This configuration allows for a wide continuous wavelength coverage from 0.8 to 2.5 μm, divided over six orders, and yields a resolution of $R \sim 1000$. The observing setup was similar to that described for FIRE observations. Because of the higher resolution for GNIRS, higher per-frame exposure times of between 240 and 300 s were chosen. The slit was positioned at the parallactic angle at the beginning of each observation. An A0V star was also observed after each set of science observations for telluric and flux calibration.

The GNIRS data were calibrated and reduced using the `XDGNIRS` pipeline, which was specifically developed to reduce GNIRS cross-dispersed data. The pipeline is partially based on the `REDCAN` pipeline for reduction of mid-IR imaging and spectroscopy from CANARICAM on the Gran Telescopio Canarias (González-Martín et al. 2013). The steps began with pattern
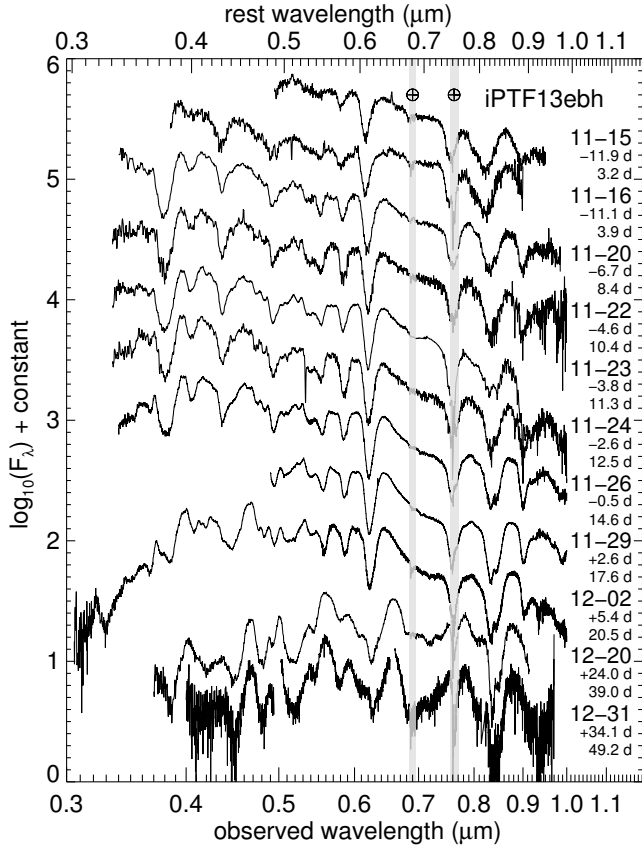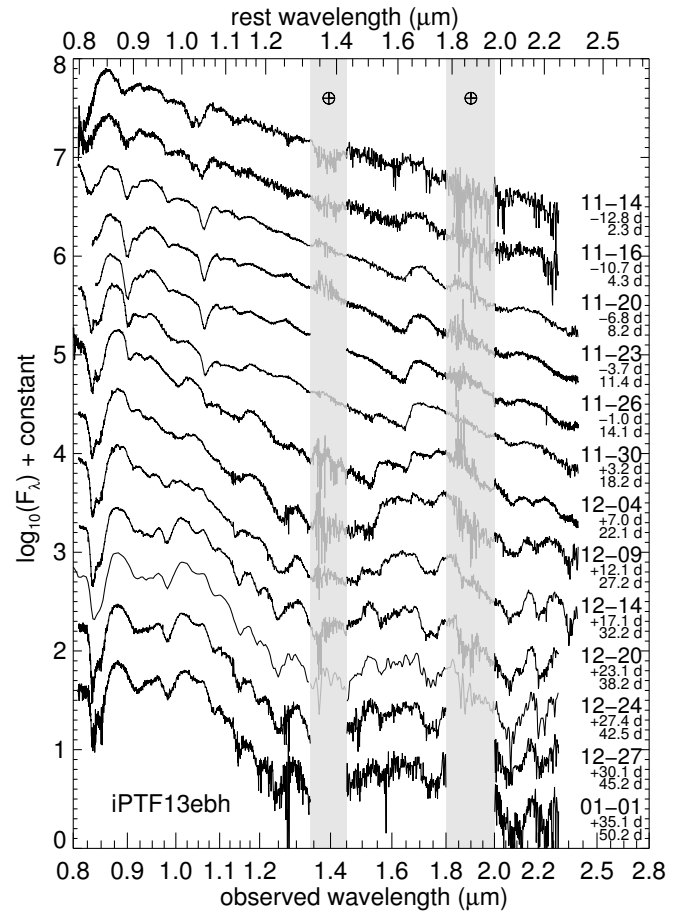
Fig. 3. Optical spectra of iPTF13ebh. The UT date of observation, phase relative to explosion and phase relative to *B*-band maximum are labeled for each spectrum. The gray vertical bands mark the regions of the strongest telluric absorptions.

noise cleaning, nonlinearity correction, locating the spectral orders, and flat-fielding. Sky subtractions were performed for each AB pair closest in time, then the 2D spectra were stacked. Spatial distortion correction and wavelength calibrations were applied before the 1D spectrum was extracted. To perform telluric correction, the stellar hydrogen lines were first removed from the telluric star spectrum. The IRAF[2] task `telluric` then interactively adjusted the relative wavelength shift and flux scale to divide out telluric features present in the science spectrum. A blackbody spectrum was then assumed for the telluric star for the flux calibration. Finally, the six orders were joined to form a single continuous spectrum.

The SpeX spectrum was obtained in the single-prism low-resolution (LRS) mode. In this configuration, SpeX yields an uninterrupted wavelength coverage from ~0.7 to 2.5 μm and a resolution of $R \sim 200$. The same ABBA nod-along-the-slit technique was used to obtain 12 frames of 150-s exposures, totaling 30 min of on-target integration time. The details in the observation and reduction procedures can be found in Cushing et al. (2004) and Marion et al. (2009).

3. Photometric properties

The photometric properties of a SN Ia serve as useful indicators of possible peculiarities. We used the preliminary Swope

---

Fig. 4. NIR spectra of iPTF13ebh. The UT date of observation, phase relative to explosion and phase relative to *B*-band maximum are labeled for each spectrum. The gray vertical bands mark the regions of the strongest telluric absorptions.

light curves (without host galaxy subtractions) and pre- and post-discovery images from P48 to establish some basic light-curve parameters for iPTF13ebh.

The earliest data points in the *r*-band light curve from P48 and Swope allow for an accurate explosion time estimation. We used a Markov chain Monte Carlo code to determine the time of explosion and the associated uncertainty. The exponent is treated as a free parameter to allow for deviations from the t^2 fireball regime (e.g., Zheng et al. 2014; Goobar et al. 2015). The time of explosion for iPTF13ebh is determined to be between the earliest detection and the non-detection image the night before, on 2013 November 11.85 UT or $\mathrm{JD}_{explosion} = 2\,456\,608.4 \pm 0.2$. That is 0.59 day after the non-detection, 0.36 day before the first detection, 1.30 days before the discovery image, and 2.29 days before the first NIR spectrum. The result is robust against varying the number of light-curve points included in the calculations. The resulting exponent is 1.5 ± 0.1, which is substantially different from the fireball regime and the average exponents determined using large samples of SN Ia light curves (e.g., Conley et al. 2006; Hayden et al. 2010; Firth et al. 2015).

To test the effect of host subtraction on the time of explosion, we subtracted the 180-degree rotated image of the host from each Swope *r*-band image. The host, NGC 890, is morphologically classified as an SAB galaxy (de Vaucouleurs et al. 1991), and its projected shape in the plane of the sky is assumed to have axial symmetry (Fig. 1). The resulting subtracted
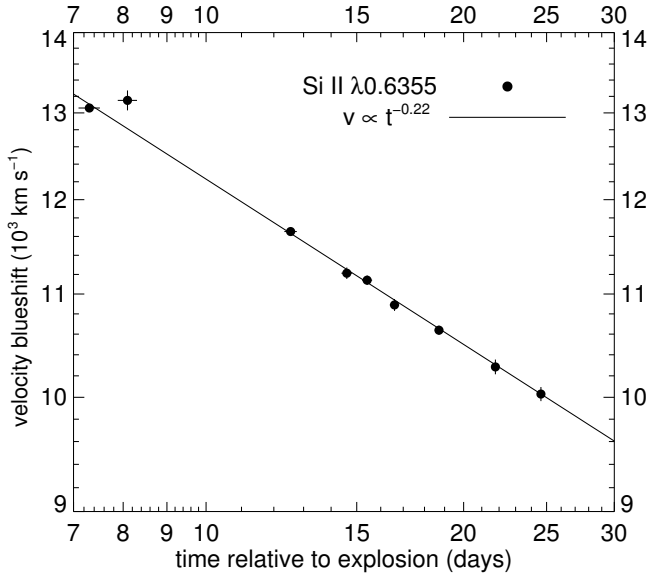
Fig. 5. Si II $\lambda 0.6355$ μm velocity time evolution and $v \propto t^{-0.22}$ power law fit of Piro & Nakar (2013). The -0.22 exponent yields an excellent fit to the data. The inferred explosion time is 19.2 ± 0.2 days before B maximum.

r-band P48 and Swope light curve was again analyzed with the Markov chain Monte Carlo code. The time of explosion, $2\,456\,608.2 \pm 0.2$, is fully consistent with what we found using the subtracted P48/unsubtracted Swope light curve. This points to the importance of the earliest two P48 points for the determination of the explosion time.

As a comparison to measuring the explosion time with the *r*-band light curve, we also constrained the explosion time with a fit of the $v \propto t^{-0.22}$ power law of Piro & Nakar (2013) to the Si II $\lambda 0.6355$ μm velocity time evolution (Fig. 5). If this velocity-inferred explosion time is earlier than the one measured from the light curve, it may indicate that the supernova had a dark phase in which it was initially too dim to be observed because of the delay between the explosion time and the time when the heating from ^{56}Ni first reached the outer ejecta (Piro & Nakar 2013). The best-fit explosion time with the -0.22 exponent is 19.2 ± 0.2 days before B maximum. As shown in Fig. 5, the -0.22 exponent yields an excellent fit to the data. Treating the exponent as a free parameter yields a consistent explosion date and the same exponent of -0.22. This inferred explosion time implies a dark phase of ~ 4 days and that the ^{56}Ni is concentrated to the center of the ejecta. Note that the uncertainty in the explosion date only reflects the goodness of the power-law fit to the data and does not take into account any approximations used to obtain Eq. (13) in Piro & Nakar (2013). It is interesting, however, to note that this dark phase is considerably longer than those of SNe 2009ig, 2011fe, and 2012cg considered in Piro & Nakar (2014).

Several light-curve parameters are determined here using the Swope optical and RetroCam NIR light curves. The B-band light curve decline rate, $\Delta m_{15}(B)$ (Phillips 1993) is a luminosity indicator, but is also found to be an indicator of the strength of some spectral features in the optical (e.g., Nugent et al. 1995) and NIR (e.g., Hsiao et al. 2013). The color-stretch parameter s_{BV}, another a luminosity indicator, is found to better distinguish among the fast-declining events than $\Delta m_{15}(B)$ (Burns et al. 2014). Since the Swope light curves are so densely sampled and have good data quality, we elected to interpolate the light curves using

Table 7. Summary of the basic properties of iPTF13ebh.

α (J2000)	$02^h21^m59^s.98$
δ (J2000)	$+33°16'13''.7$
$JD_{explosion,r}{}^a$	$2\,456\,608.4 \pm 0.2$
$JD_{explosion,Si\,II\,v}{}^b$	$2\,456\,604.2 \pm 0.2$
$JD_{max}(B)$	2456623.4 ± 0.1
$\Delta m_{15}(B)$	1.79 ± 0.01
s_{BV}	0.63 ± 0.02
host	NGC 890
heliocentric redshift	0.0133
distance modulus^c	33.63 ± 0.18
$E(B-V)_{host}$	0.05 ± 0.02
$m_{u,max}{}^d$	15.29 ± 0.05
$m_{B,max}{}^d$	14.68 ± 0.05
$m_{V,max}{}^d$	14.62 ± 0.04
$m_{g,max}{}^d$	14.60 ± 0.04
$m_{r,max}{}^d$	14.64 ± 0.04
$m_{i,max}{}^d$	15.11 ± 0.03
$m_{Y,max}{}^d$	14.90 ± 0.02
$m_{J,max}{}^d$	14.88 ± 0.02
$m_{H,max}{}^d$	15.04 ± 0.01
$M_{u,max}$	-18.34 ± 0.19
$M_{B,max}$	-18.95 ± 0.19
$M_{V,max}$	-19.01 ± 0.18
$M_{g,max}$	-19.03 ± 0.18
$M_{r,max}$	-18.99 ± 0.18
$M_{i,max}$	-18.52 ± 0.18
$M_{Y,max}$	-18.73 ± 0.18
$M_{J,max}$	-18.75 ± 0.18
$M_{H,max}$	-18.59 ± 0.18

Notes. $^{(a)}$ Derived from *r*-band light curve. $^{(b)}$ Derived from the fit of the $v \propto t^{-0.22}$ power law of Piro & Nakar (2013) to the Si II $\lambda 0.6355$ μm velocity time evolution. $^{(c)}$ The distance modulus is derived from the host recession velocity, which is corrected for the influence of the Virgo cluster, the Great Attractor, and the Shapley supercluster (Mould et al. 2000). The error includes uncertainties from peculiar velocity. $^{(d)}$ The peak magnitudes include reddening correction for the foreground Milky Way and the host extinction.

Gaussian processes (Rasmussen & Williams 2006), and directly measured $\Delta m_{15}(B)$, s_{BV}, and the time of B maximum. They are listed in Table 7. SNooPy fits (Burns et al. 2011) yield consistent values for these parameters. The time of B-band maximum determined here is consistent with that found by Wyrzykowski et al. (2014), but with much higher precision. We also measured the host color excess and the host/Milky Way extinction-corrected peak magnitudes using SNooPy color-stretch fits and the intrinsic color loci presented in Burns et al. (2014). These values are summarized in Table 7.

The $\Delta m_{15}(B)$ value of 1.79 places iPTF13ebh in the category of a fast-declining SN Ia, but its photometric and spectroscopic properties are not quite as extreme as subluminous or 91bg-like SNe Ia. Unlike 91bg-like objects, the primary maxima of the NIR *iYJH* light curves peak before the B maximum. The secondary maxima are present in all *iYJH*-bands. Its B and V absolute magnitudes fall within the width-luminosity relations presented in Phillips et al. (1999). It is therefore categorized as a transitional event. In this category, iPTF13ebh is one of the best observed and one of the most extreme members, pushing toward the boundary between transitional and subluminous/91bg-like objects. We explore the subject of transitional events in more detail and propose concrete definitions for this group in Sect. 6.
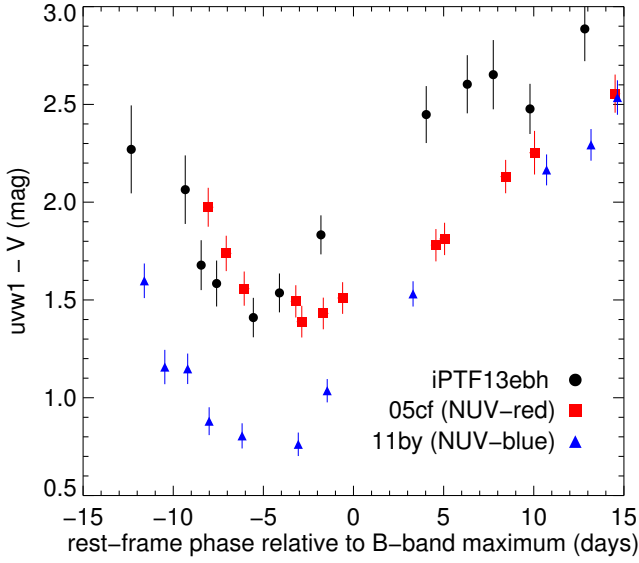
Milne et al. (2013) observed an apparent bimodality based on UV-to-optical colors and UV spectroscopic properties. Two main groups were identified to be NUV-blue and NUV-red. It was also noted that the vast majority of the SNe Ia with optical carbon detections (classified based on optical C II lines) belong to the NUV-blue group. iPTF13ebh would have been classified as a narrow-peaked SN Ia and thus excluded from the analysis of normal SNe Ia by Milne et al. (2013). Nonetheless, we examined the UV color as it appears to be a strong indicator of the appearance of carbon. Because we lack UV spectra, K-corrections were not applied to our UV light curves, following the same analysis as Milne et al. (2013). The $uvw1 - V$ color curve of iPTF13ebh is quite red and remains well above 1.0 mag before B maximum (Fig. 6). This certainly places iPTF13ebh in the NUV-red territory. However, note that the $uvw1 - V$ color curve of iPTF13ebh evolves faster than that of a typical NUV-red SN Ia (Fig. 6). This is the subject of ongoing work by Milne et al. (in preparation).

iPTF13ebh may provide a rare example of carbon detection in a NUV-red SN Ia. The optical C II of iPTF13ebh is weak and disappears quickly (Sect. 4.3), while the NIR C I is strong early (Sect. 4.2). It weakens quickly, but persists until maximum light. In a typical SN Ia spectroscopic follow-up in the optical, starting more than a week past the explosion date, the unburned carbon would have been missed. Carbon studies based on optical C II features would then introduce a bias. A larger sample of NIR spectra is needed to firmly conclude whether this bias results in the observed association of unburned carbon with NUV-blue SNe Ia.

4. NIR carbon detections and evolution

The pre-maximum spectra of iPTF13ebh were analyzed using the automated spectrum synthesis code SYNAPPS (Thomas et al. 2011b), derived from SYNOW (Branch et al. 2005). SYNAPPS uses a highly parameterized and therefore fast spectrum synthesis technique, which is useful for identifying the ions that form the observed features. It has been employed successfully to identify
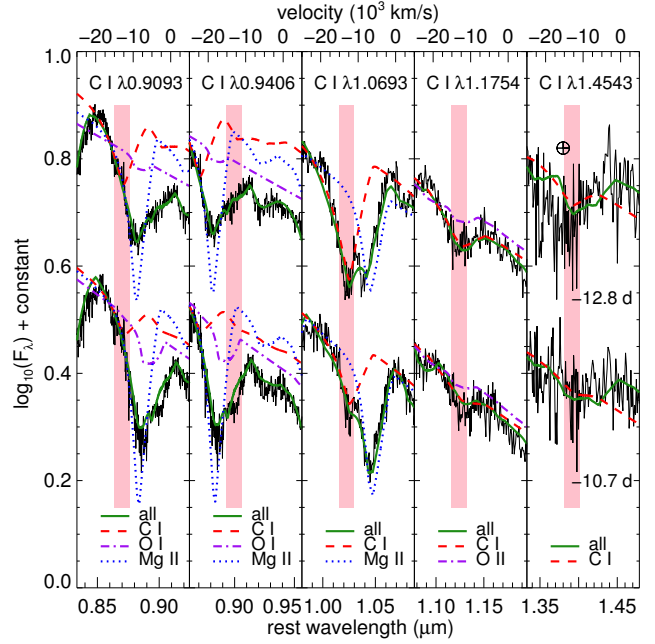
Fig. 7. NIR C I lines of iPTF13ebh in the two earliest spectra. The phase relative to the time of B maximum is labeled for each spectrum. The best-fit SYNAPPS models for both epochs yielded a velocity of 13 000 km s^{-1} for C I, representing the base of the line-forming region. The best fit as a whole and the isolated contributions from the main ions responsible for the spectral features in each wavelength region are plotted. A vertical band marks this velocity for each C I line. C I $\lambda 1.4543\,\mu$m for iPTF13ebh is located near the region of strong telluric absorption, which is identified with an Earth symbol.

the C II $\lambda 0.6580\,\mu$m lines in early optical spectra (Thomas et al. 2007, 2011a; Parrent et al. 2012) and the C I $\lambda 1.0693\,\mu$m lines in NIR spectra taken near maximum light (Hsiao et al. 2013; Marion et al. 2015).

4.1. Carbon detections in the NIR

In the two earliest NIR spectra of iPTF13ebh (-12.8 and -10.7 days with respect to B maximum), the C I $\lambda 1.0693\,\mu$m feature is prominent. SYNAPPS was employed to confirm the identification and to analyze each NIR C I line in detail. Several NIR C I lines are identified at a velocity of $-13\,000$ km s^{-1}, representing the base of the line-forming region. They are presented in Fig. 7. C I $\lambda 0.9093\,\mu$m is listed as the second strongest NIR C I line in Table 5 of Marion et al. (2009), and it is detected as weak notches in both spectra. The C I $\lambda\lambda 0.9406, 1.1754\,\mu$m lines appear to be present in the spectra, but some blending makes the identification less secure. C I $\lambda 1.4543\,\mu$m appears isolated from other ions; however, the proximity to the strong telluric absorptions between the J and H-band makes this feature unsuitable for the search of unburned carbon. C I $\lambda 1.0693\,\mu$m, on the other hand, forms one of the strongest features in these early NIR spectra, even comparable to the strength of the Mg II $\lambda 1.0927\,\mu$m feature, which is usually the most prominent feature in this wavelength region for SNe Ia.

Echoing past works, such as Marion et al. (2006), we can confirm here that C I $\lambda 1.0693\,\mu$m is the best NIR feature for carbon detection. All the other C I lines shown here overlap with other lines or telluric features. For a second line to confirm the presence of C I, we recommend C I $\lambda 1.1754\,\mu$m. This feature is
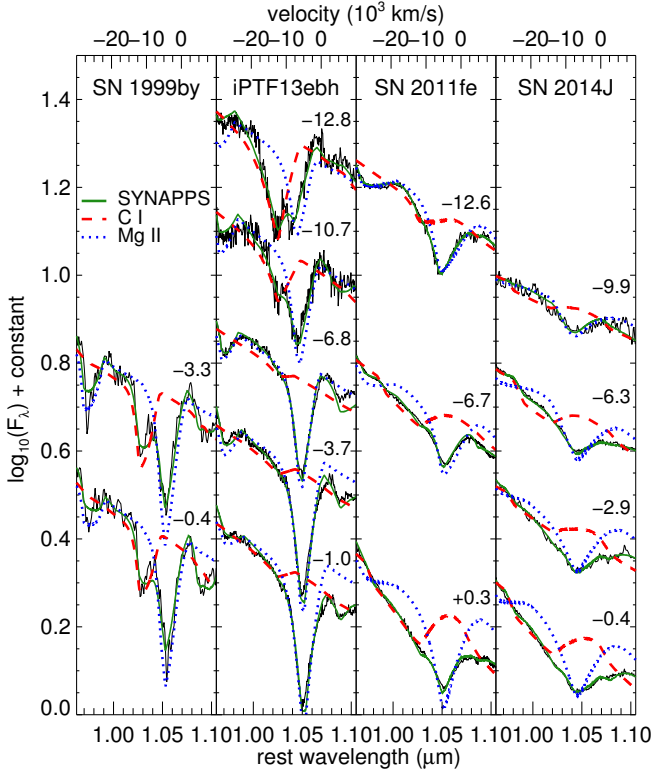
Fig. 8. NIR C I $\lambda1.0693$ μm line for four SNe Ia with NIR C I detection. Each panel presents the time evolution for each supernova with the phase relative to B maximum labeled for each spectrum. The solid green curves are the best-fit SYNAPPS models. Dashed red and dotted blue curves show the isolated contributions from C I $\lambda1.0693$ μm and Mg II $\lambda1.0927$ μm, respectively. The velocity axes on the top are plotted with respect to the C I $\lambda1.0693$ μm line.

detected in both iPTF13ebh and SN 1999by (Höflich et al. 2002), and is tentatively identified in SN 2011fe (Hsiao et al. 2013). It is the second strongest C I line present in the NIR spectra of SN 1999by. The line blending effect with the O II $\lambda1.1667$ μm feature is expected to be weak because neutral oxygen is the dominant ionization state and the O II $\lambda1.1667$ μm line strength is intrinsically weak.

4.2. Comparison to other SNe Ia

So far, NIR C I has been detected in only four SNe Ia; these are plotted in Fig. 8 for comparison. The first such detection is in the 91bg-like SN 1999by. Höflich et al. (2002) presented NIR spectra of SN 1999by with strong C I $\lambda1.0693$ μm that persisted through maximum light. The morphology of the feature is similar to that of iPTF13ebh, but the C I $\lambda1.0693$ μm feature of iPTF13ebh weakens rapidly and all but disappears by maximum light. The subluminous delayed-detonation model of Höflich et al. (2002) also predicts a very strong C I $\lambda0.9406$ μm line. For the NIR spectra of SN 1999by, the C I $\lambda0.9406$ μm line falls outside the observed wavelength region so that the prediction was not tested. The NIR spectra of iPTF13ebh include the C I $\lambda0.9406$ μm feature, but as seen in Fig. 7, the feature is not strong.

SN 2011fe, discovered within one day of the explosion, has been shown to be a proto-typical SN Ia (e.g., Nugent et al. 2011; Parrent et al. 2012). Hsiao et al. (2013) interpreted the flattened emission wing of Mg II $\lambda1.0092$ μm as caused by

C I $\lambda1.0693$ μm. It was shown to increase in strength toward maximum light (Fig. 8). We note that the profiles and the behaviors of the C I features of SN 2011fe and iPTF13ebh are drastically different. While the C I line strength increases toward maximum light for SN 2011fe, the C I line in iPTF13ebh is strong, but decreases in strength rapidly soon after explosion. iPTF13ebh is the only one of the four SNe Ia with detected C I that shows this behavior. We note that while the first two spectra of iPTF13ebh exhibit C I profiles similar to those of SN 1999by, subsequent spectra show only traces of C I, manifested in the flattened wing of Mg II $\lambda1.0092$ μm, much like the C I line profile of SN 2011fe.

SN 2014J developed a very similar C I line profile to that of SN 2011fe. Indeed, as mentioned by Hsiao et al. (2013), the flattened wing of Mg II $\lambda1.0092$ μm is a common characteristic of normal-bright SNe Ia. Marion et al. (2015) showed a possible detection of C I in the SYNAPPS fit of the maximum-light NIR spectrum. Here we take advantage of the densely cadenced observations of SN 2014J to show the evolution of the C I feature. The SYNAPPS fits in Fig. 8 suggest a moderate increase in strength. Unfortunately, the late discovery of SN 2014J (Zheng et al. 2014; Goobar et al. 2014) did not permit the early spectroscopic follow-up that is required to clearly show the increase in C I strength, as was shown in SN 2011fe (Hsiao et al. 2013).

SN 2014J has been shown to be a normal SN Ia, with significant reddening associated with a large amount of dust (Amanullah et al. 2014; Foley et al. 2014; Brown et al. 2014b), and relatively high velocity for Si II $\lambda0.6355$ μm (Marion et al. 2015) that places the supernova near the boundaries between the normal and high-velocity subclasses (e.g., Benetti et al. 2005; Wang et al. 2009). In large samples of optical spectra, Folatelli et al. (2012) and Silverman & Filippenko (2012) both observed that SNe Ia with carbon tend to have lower Si II velocities, while the objects without carbon span the entire range of Si II velocities. This phenomenon may be a result of the difficulty in detecting C II $\lambda0.6580$ μm at high velocities where it overlaps with the Si II $\lambda0.6355$ μm line. The detection of NIR C I $\lambda1.0693$ μm in the moderately high velocity SN 2014J shows that searching for signatures of unburned carbon in the NIR may remedy this observational bias. We explore the differences in NIR C I and optical C II lines in more detail in the following subsection.

In Fig. 9, we compare the C I velocity evolution for the four SNe Ia with C I detections. As the location of the C I line minimum in most cases cannot be directly measured (Fig. 8), we plot the C I velocities, representing the base of the line-forming region from the best-fit SYNAPPS models. They therefore have no associated uncertainties. For both iPTF13ebh and SN 1999by, the C I velocity evolution is flat (although, SN 1999by does not have early-phase data to rule out an early decline). The line-forming region probes the inner carbon-rich layers. For SNe 2011fe and 2014J, the C I velocities continue to decline until only a few days before maximum. Parrent et al. (2011) presented the C II-to-Si II velocity ratio measured from a sample of optical spectra and showed flat time evolution and a ratio of ~1.1 for the majority of the SNe Ia studied. iPTF13ebh certainly falls outside of this norm, with a varying C I-to-Si II velocity ratio increasing from ~1 to ~1.3.

4.3. Comparison of NIR C I and optical C II

The search for unburned material in SNe Ia has largely been focused on optical wavelengths and principally on the C II $\lambda0.6580$ μm feature, which disappears quickly a few days past explosion. The recent detections of the NIR C I $\lambda1.0693$ μm
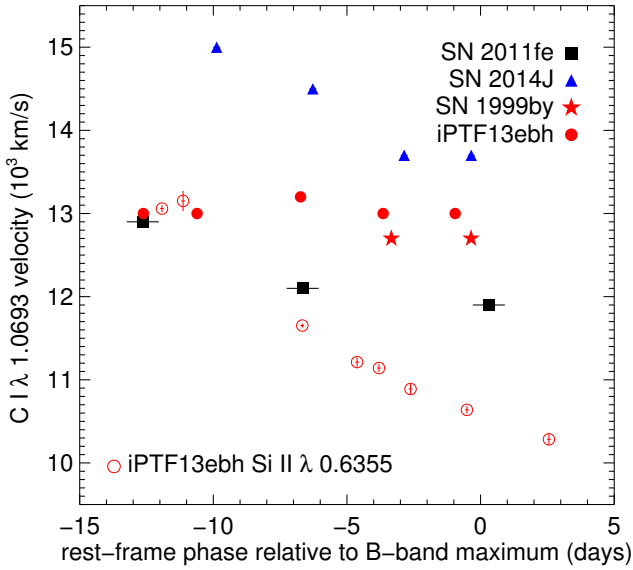
Fig. 9. Time evolution of the C I $\lambda 1.0693$ μm velocities for the four supernovae with C I detections. Various symbols represent different objects as noted. Blue, black, and red symbols represent SNe Ia with optical light-curve decline rates in the range $\Delta m_{15}(B) < 1.0$, $1.0 < \Delta m_{15}(B) < 1.6$, $\Delta m_{15}(B) > 1.6$, respectively. The velocities are taken from the C I velocity representing the base of the line-forming region in the best-fit SYNAPPS models. The Si II $\lambda 0.6355$ μm velocity of iPTF13ebh is also plotted for comparison.

line, still present near maximum light, suggest that shifting to the NIR is a less biased way of investigating unburned material. In this section, we compare the NIR C I and optical C II features for the four SNe Ia with reported NIR C I detection.

In Fig. 10, we compare the NIR C I and optical C II features of iPTF13ebh as inferred by the SYNAPPS models. As mentioned in the previous subsection, the NIR C I of iPTF13ebh is the strongest ever observed, but weakens rapidly in dramatic contrast to the behavior of the NIR C I lines of SNe 2011fe and 2014J. The first two NIR spectra, taken at -12.8 and -10.7 days relative to B maximum, both show a strong C I $\lambda 1.0693$ μm line, and there is evidence for a weak C II $\lambda 0.6580$ μm line in the first two optical spectra taken at -11.9 and -11.1 days relative to B maximum. In the classification scheme of Folatelli et al. (2012), the C II $\lambda 0.6580$ μm feature would be classified as F for flat Si II $\lambda 0.6355$ μm emission, and not as A for a clear carbon absorption. The optical C II line also weakens rapidly. Both the weak optical C II and the strong NIR C I features appear at approximately the same epoch. It is possible that the optical C II feature was stronger at an even earlier epoch, then later yielded to the growing C I as a result of recombination.

We now consider the optical C II lines for other SNe Ia with NIR C I detections. The optical spectra of SN 1999by from Garnavich et al. (2004) and Matheson et al. (2008) showed no strong C II features from -5 days through to maximum light, while the NIR spectra of Höflich et al. (2002) showed strong detections of several C I features during the same phases. The optical C II $\lambda 0.6580$ μm feature was detected in SN 2011fe (Parrent et al. 2012), and is weaker than the NIR C I, especially at maximum light (Hsiao et al. 2013). The NIR C I is weak early on, but gradually increases in strength up until maximum light. While C I was detected in several pre-maximum NIR spectra of SN 2014J (Marion et al. 2015), C II was not detected in the optical spectra taken during the same phases (Goobar et al. 2014).

These optical C II and NIR C I comparisons are summarized in Fig. 10, along with the SYNAPPS fits and the illustration of the C I and C II contributions.

While the line profile, strength and time evolution of the NIR C I lines are drastically different in iPTF13ebh, SN 1999by, and normal SNe Ia like SNe 2011fe and 2014J, the common theme is that except at the very early epochs, the strength of the NIR C I lines is *always* observed to be much stronger than that of their optical C II counterparts (Fig. 10). The laboratory line strength of C II $\lambda 0.6580$ μm is a few orders of magnitude stronger than that of C I $\lambda 1.0693$ μm at a reasonable range of temperature. The observations of stronger NIR C I lines indicate that SN Ia, regardless of their luminosity, produce conditions in the outer layers that are favorable to a much higher abundance of C I than C II. This appears to contradict the prediction by Tanaka et al. (2008), that the dominant carbon ionization state in the outer parts of the ejecta is C II.

Four C I detections is obviously too small a sample to reach a firm conclusion. However, we note here that the small number of C I detections is not due to the lack of or weak C I in SNe Ia, but to the small sample size of pre-maximum NIR spectra. The most recent analyses of SN Ia NIR spectroscopy have all revealed C I $\lambda 1.0693$ μm to be present (Hsiao et al. 2013; Marion et al. 2015; Stritzinger et al. 2015)

5. Other spectroscopic properties

In addition to probing unburned material in the ejecta, early time-series NIR spectra provide measures of several physical parameters in SN Ia explosions (Wheeler et al. 1998). Hsiao et al. (2013) introduced quantitative measurements for the H-band break and Mg II velocity. We explore these quantities and other spectroscopic properties of iPTF13ebh in this section.

5.1. Optical spectroscopic properties

Pseudo-equivalent widths (pEW) have been widely adopted as a tool for quantifying supernova spectral features. We measured the pEW of several optical spectral features of iPTF13ebh near maximum light in the same fashion as Folatelli et al. (2013). In particular, the pEW measurements of the Si II $\lambda\lambda 0.5972$, 0.6355 μm lines are 48.9 ± 0.6 Å and 125.2 ± 0.5 Å, respectively. First introduced by Nugent et al. (1995), the R(Si II) ratio is defined as the ratio of the depth of the Si II $\lambda\lambda 0.5972$, 0.6355 μm lines and was shown to correlate with the peak luminosities of SNe Ia. A similar correlation had been shown between the pEW ratio of the same features and light-curve decline rate (Blondin et al. 2012; Folatelli et al. 2013). The Si II pEW ratio of iPTF13ebh fits other fast-declining SNe Ia in this correlation well.

Using the definition given by Folatelli et al. (2013), iPTF13ebh is placed firmly in the cool category of Branch et al. (2006), for pEW(Si II 0.5972) > 30 Å. The maximum light absorption complex near 0.43 μm is attributed to Mg II and Fe III in normal SNe Ia. This feature is dominated by strong Ti II absorptions in the spectra of 91bg-like events. Folatelli et al. (2013) named the pEW of this feature pEW3 and defined "extreme cool" (eCL) events to have $pEW3 > 220$ Å. This group of SNe Ia is largely comprised of 91bg-like events, where heavy Ti II absorptions increase pEW3 drastically. For iPTF13ebh, pEW3 is measured to be 104 ± 1 Å, confirming the weakness of Ti II. SYNAPPS fits are also performed on the pre-maximum optical spectra of iPTF13ebh. The complex near 0.43 μm described

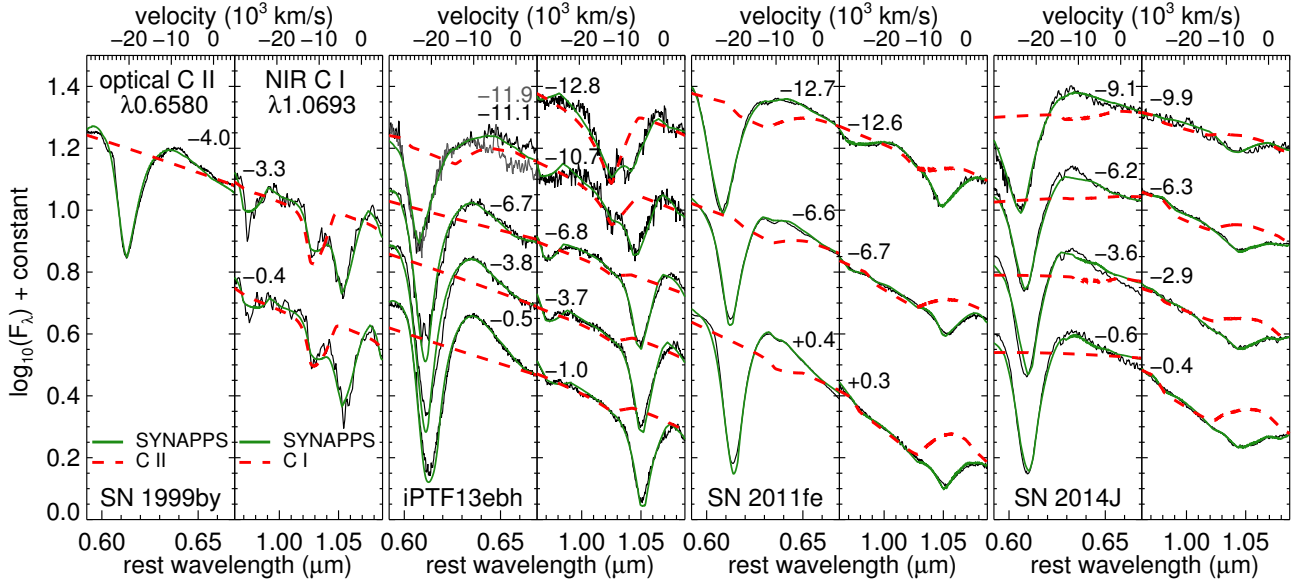**Fig. 10.** Comparison between the optical C II $\lambda 0.6580\,\mu$m and the NIR C I $\lambda 1.0693\,\mu$m lines of the four SNe Ia with C I detections. The optical/NIR pair is selected such that the spectra are close in phase for each SN Ia. The phases relative to B maximum are labeled. The velocity axes are plotted with respect to each carbon line. Since the two earliest optical spectra of iPTF13ebh are taken less than one day apart and have identical Si II/C II line profiles, they are plotted together. The SYNAPPS fit was done on the day -11.1 spectrum. Except at the very early epoch of SN 2011fe, the NIR C I line is always stronger than the optical C II line.
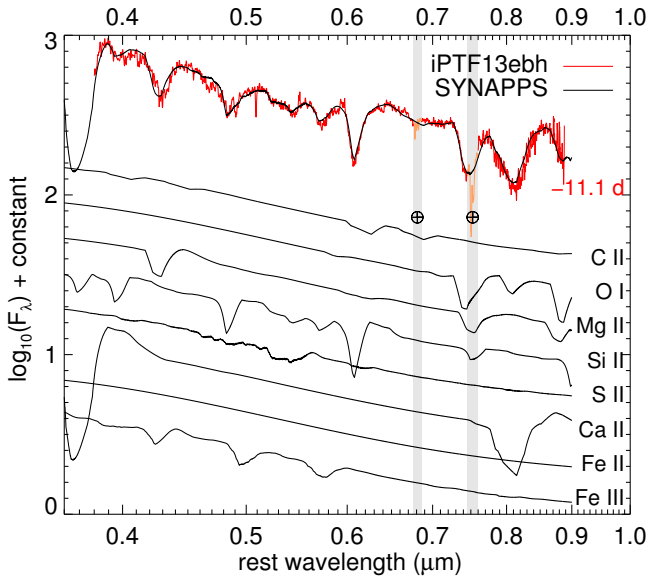
Fig. 11. SYNAPPS fit of the early optical spectrum of iPTF13ebh, taken at 11.1 days before B maximum. Isolated contributions from ions included in the fit are also shown.

above is attributed to Mg II, Fe III, and to a lesser extent, Si III (Fig. 11). No Ti II contribution is required to account for the observed profiles.

High-velocity Ca II triplet absorption features have been a topic of interest. Interpreted as a density enhancement in the outer region, the presence of high-velocity Ca II could be a signature of circumstellar material bound in the progenitor system that was swept up during the explosion (Gerardy et al. 2004). Mazzali et al. (2005) observed that almost all SNe Ia with early spectra show high-velocity Ca II. The question is: whether for the few SNe Ia that do not show high-velocity Ca II they would show high-velocity Ca II if an early spectrum

were available? iPTF13ebh is discovered exceptionally young with the first optical spectrum obtained 3.2 days past explosion. (The Ca II triplet is present in the NIR spectra, but the detached high-velocity component, if present, would be outside of the wavelength coverage.) SYNAPPS fits for all pre-maximum optical spectra show that only a photospheric component is required to yield excellent fits to the observed Ca II triplet near 0.8 μm. (See Fig. 11, for example.) For iPTF13ebh, there is no evidence of a detached high-velocity Ca II feature as early as 3.2 days past explosion. This agrees with previous results that low-luminosity SNe Ia are less likely to show strong detached high-velocity Ca II features at early times (Hsiao 2009; Childress et al. 2014; Maguire et al. 2014).

5.2. Delayed-detonation model

Höflich et al. (2002) constructed a set of delayed-detonation (e.g., Khokhlov 1991) models that span the range of normal-bright to subluminous SNe Ia. For iPTF13ebh, we selected the model with a deflagration-to-detonation transition density of $\rho_{tr} = 16 \times 10^6$ g cm^{-3}, which synthesized 0.268 $M_\odot$ of ^{56}Ni. The choice is based on the peak absolute brightness and decline rate of iPTF13ebh, with no further fine-tuning to match the model to the observed spectra. The model yields a peak absolute magnitude in B of -18.22 mag, a decline rate in B of $\Delta m_{15}(B) = 1.82$, and the rise time between the time of explosion and B maximum of 15.4 days, comparable to the observed values for iPTF13ebh (Table 7).

To calculate the explosions, light curves, and spectra, we used the radiation transport code HYDRA, which includes hydrodynamic solvers, Eddington tensor and Monte Carlo methods for low-energy photon, gamma-ray, and positron transport, and time-dependent, nuclear and atomic networks (Höflich 1990, 2002, 2009; Höflich et al. 1995; Penney & Höflich 2014). The synthetic light curves and spectra were recomputed using updated atomic data from De et al. (2010) and Friesen et al. (2014) as described in Diamond et al. (2014) and Telesco et al. (2015).
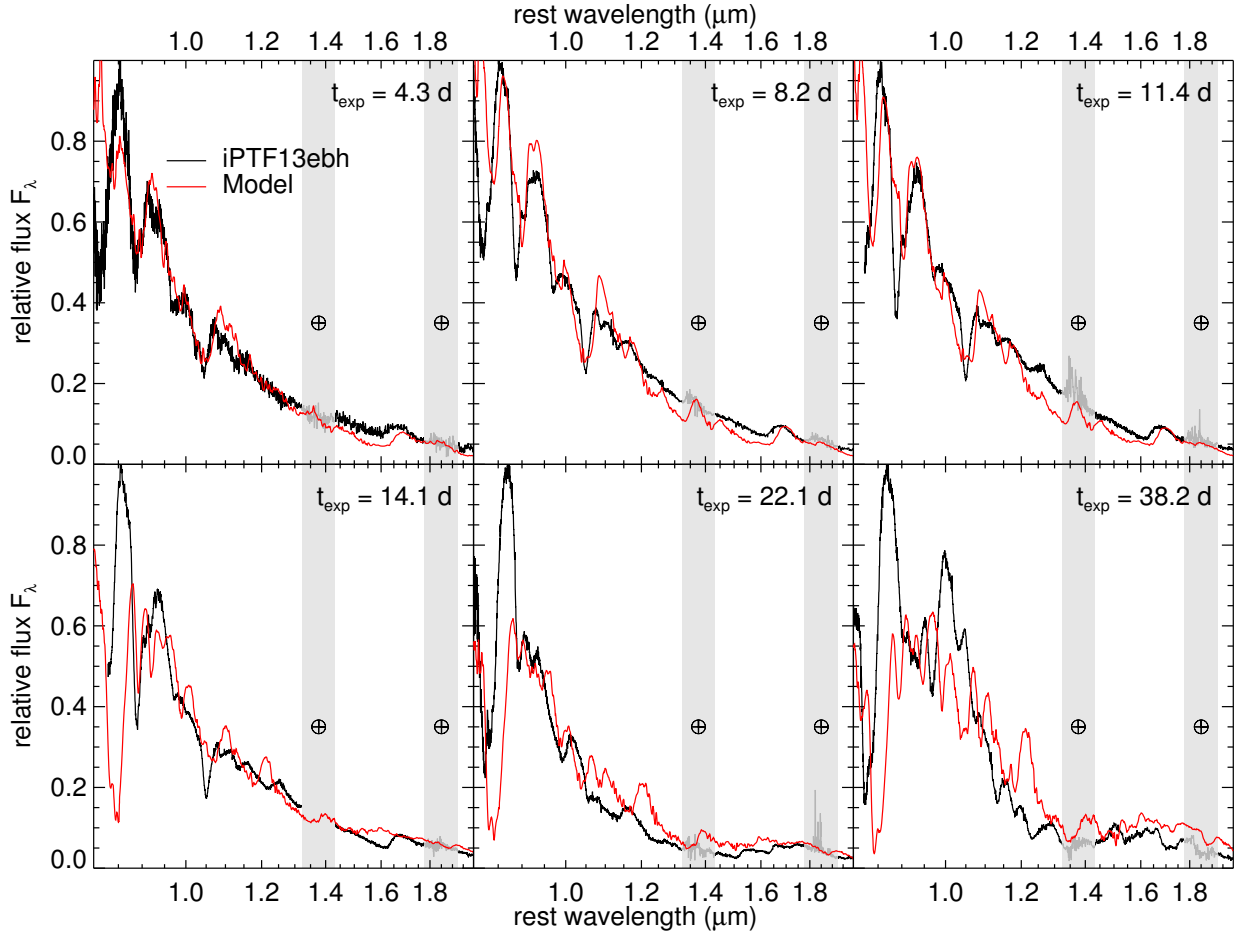
Fig. 12. Comparison between the NIR spectra of iPTF13ebh and the $\rho_{tr} = 16 \times 10^6$ g cm^{-3} model spectra. The phases of the observed spectra are noted in the plot. These are relative to the explosion date, as inferred from the early-time r-band light curve. The model spectra are computed at these epochs.

In Fig. 12, the iPTF13ebh and the $\rho_{tr} = 16 \times 10^6$ g cm^{-3} model spectra are compared between 4 and 38 days past explosion. The line identifications are similar to those given in Wheeler et al. (1998) and Höflich et al. (2002). At early epochs, the spectra are dominated by blends of C I, O I, Mg II, Si II, Ca II, and singly-ionized elements in the iron group. The strong feature at ~0.9 μm is identified as Mg II $\lambda\lambda$0.9218, 0.9244 μm, O I λ0.9266 μm, and C I $\lambda\lambda$0.9406, 0.9658 μm. And the feature at ~1.05 μm is identified as C I λ1.0693 μm and Mg II $\lambda\lambda$1.0914, 1.0951 μm (named Mg II λ1.0927 μm in other sections). The feature at ~1.35 μm is identified as Si II λ1.3650 μm. Between 8 and 11 days after the explosion (top panels of Fig. 12), the feature at 1.05 μm becomes too broad with the emission wing too strong in the model compared to the observations. This feature is produced by Mg II, with contributions from C I on the blue side and the suppression of the emission component due to iron-group elements on the red side. Increasing the ^{56}Ni abundance in the outer ejecta would have two desired effects: higher ionization, which would lead to decreased contribution from C I, and a stronger suppression on the emission wing from the iron-group elements. These may be achieved through a brighter model, stronger outward mixing of ^{56}Ni, or higher progenitor metallicity. Note that the ionization of carbon is sensitive to changes in transition density only for models in this range of brightness.

In general, the influence of iron-peak elements increases with time as the spectrum-formation region probes deeper ejecta layers. However, the 1.05 μm region remains relatively clear of iron-peak lines before maximum, demonstrating again that the C I and Mg II lines here are ideal for studying unburned material and the boundary between carbon and oxygen burning. At later time, around and after B maximum (bottom panels of Fig. 12), the model features have much lower velocities than those of iPTF13ebh, indicating that the model has a line-forming region that recedes too fast. This suggests a need for an increase in the model ^{56}Ni production. Alternatively, the outward mixing of ^{56}Ni may increase the opacity of layers of partial burning. Note that using the explosion date inferred from a power-law fit to the Si II λ0.6355 μm velocity measurements improves the situation, but the evolution of the NIR spectral features is still much too fast in the model spectra.

At early time, less than a week past explosion, the model produces C I lines that are slightly weaker than those observed in iPTF13ebh. The ionization balance of C I and C II depends sensitively on the recombination rate and heating. C I could become stronger by enhanced density as a result of interaction with circumstellar material in the progenitor system (Gerardy et al. 2004), which increases the recombination rate, or by cooling due to early CO formation (Höflich et al. 1995). The strength of the model C I lines can also be increased by lowering the ^{56}Ni mass. However, the fast-evolving model spectra mentioned above suggests that lowering the model ^{56}Ni would cause further discrepancy between the model and observed spectra.
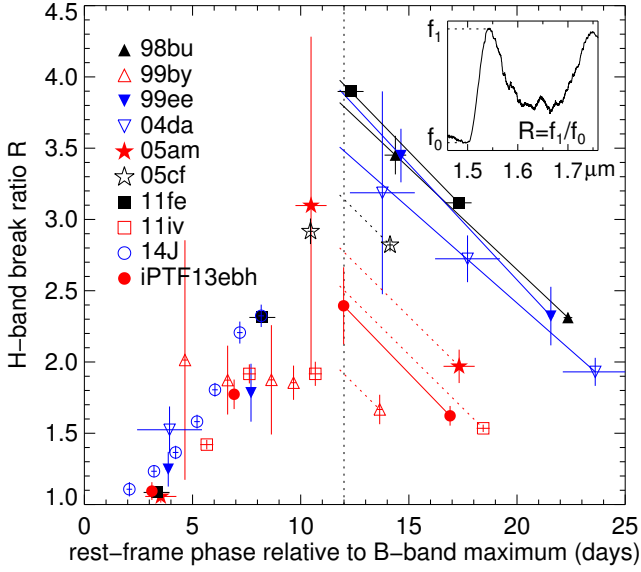
Fig. 13. Time evolution of the *H*-band break ratio. Different symbols represent measurements of different supernovae, as noted in the plot. Blue, black, and red symbols represent SNe Ia with optical light-curve decline rates in the range $\Delta m_{15}(B) < 1.0$, $1.0 < \Delta m_{15}(B) < 1.6$, $\Delta m_{15}(B) > 1.6$, respectively. The inset illustrates the definition of the *H*-band break ratio with the spectrum of SN 2011fe at 12 days past maximum. The linear fits to the post-peak decline are plotted as solid lines when more than two data points are available and as dashed lines when only a single data point is available and the error-weighted mean decline rate is assumed. There is a wide range of peak *H*-band break ratios, but the post-peak declines are remarkably uniform.

5.3. H-band iron-peak feature

The *H*-band iron-peak feature, a complex formed by Fe II/Co II/Ni II, is the most prominent spectral feature for a normal SN Ia in the NIR. First noted by Kirshner et al. (1973), it is fortuitously located in the *H*-band, in between the two strong telluric regions in the NIR, such that it is relatively well documented for nearby objects. As the interest in SN Ia cosmology in the NIR grows, understanding this spectral feature, which shifts out of the *H*-band for distant objects, becomes especially important for *K*-correction calculations (Hsiao et al. 2013; Boldt et al. 2014). The *H*-band iron-peak feature also holds the promise to provide insight into the explosion, as the strongly variable opacity provides views of very different depths at the same epoch (Wheeler et al. 1998).

Hsiao et al. (2013) defined a quantitative measure for the size of this feature. They measured the peak-to-trough flux ratios across the *H*-band break near 1.5 μm. Here, we reproduce Fig. 10 of Hsiao et al. (2013) in Fig. 13 and now include measurements for iPTF13ebh and of the recently published NIR spectra of SN 2014J (Marion et al. 2015). The flux ratios are measured consistently across the entire sample. As noted in Hsiao et al. (2013), if we exclude the data points from the peculiar SN 1999by, the rise and decline of the *H*-band break ratio is remarkably uniform. The high-cadence observations of SN 2014J show the details of the uniform monotonic rise, although the starting point appears to have occurred one day earlier than for the other SNe Ia.

The budding of the *H*-band feature for iPTF13ebh occurs around three days past maximum light, which coincides with several other SNe Ia, including SN 2011fe. There is a wide range of peak ratios; however, the post-peak decline rate of the *H*-band break ratio appears to be quite uniform. Assuming
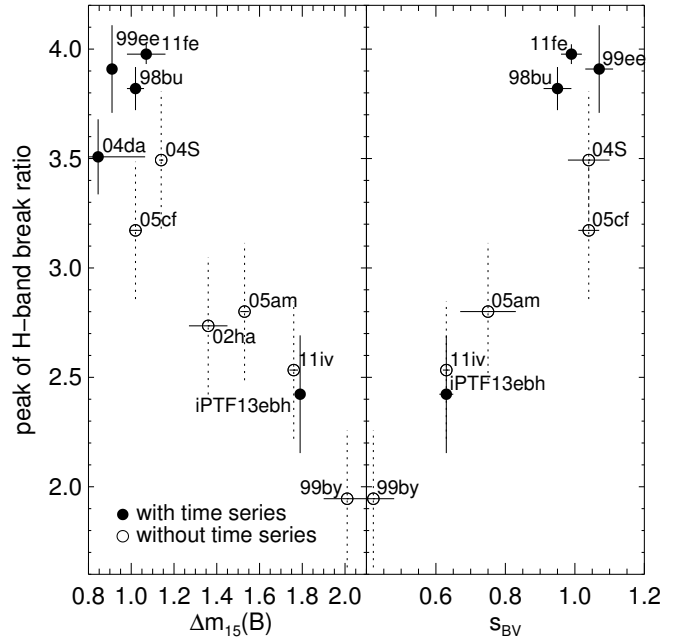

Fig. 14. Peak of *H*-band break ratio versus the optical light-curve decline rate $\Delta m_{15}(B)$ and color stretch s_{BV}. SNe Ia with two or more observations in the post-peak decline are plotted with filled circles and solid error bars, while the rest are plotted with open circles and dotted error bars. The correlations for both parameters are strong.

linear declines, the decline rates of the *H*-band break ratio for SN 2011fe and iPTF13ebh are identical within the uncertainties, -0.16 ± 0.01 day^{-1} and -0.16 ± 0.06 day^{-1}, respectively, even though the two supernovae have drastically different luminosities. The error-weighted mean decline rate determined by Hsiao et al. (2013) is -0.15 ± 0.04 day^{-1}. This value appears to be robust among SNe Ia with a wide range of luminosities. SN 2011iv, another fast-declining transitional object ($\Delta m_{15}(B) = 1.76 \pm 0.02$), shows some peculiarity in the time evolution of the flux ratio. The flux ratio appears to peak earlier than the normal 12 days past maximum inferred from available data, but the cadence is not dense enough to definitively locate the peak of the *H*-band break ratio.

Hsiao et al. (2013) noted the strong correlation between the peak *H*-band break ratio and $\Delta m_{15}(B)$. In Fig. 14, we reproduce Fig. 11 of Hsiao et al. (2013) using the same technique, with the addition of iPTF13ebh and a few other SNe Ia. We also plot the *H*-band ratio against the color-stretch parameter s_{BV} (see Burns et al. (2014) and Sect. 6). From Fig. 13 and following the same procedure as Hsiao et al. (2013), we assume that the time evolution of the *H*-band ratio reaches its peak at 12 days past *B* maximum and declines linearly thereafter. For objects with two or more post-peak measurements, the directly measured decline rate is used to extrapolate to the peak. For SNe with one post-peak measurement, we assume the error-weighted mean decline rate of -0.15 ± 0.04 day^{-1}. The correlation in Fig. 14 remains quite strong for both light-curve parameters, $\Delta m_{15}(B)$ and s_{BV}, with the addition of a few more objects.

The correlation between the *H*-band feature and light-curve decline rate (and luminosity) was first pointed out by Hsiao (2009). Using principal component analysis (PCA) on eight published NIR spectra, the PCA model showed that the SN luminosity is not only correlated with the emission strength of the *H*-band feature, but also with its width. Low-luminosity and

fast-declining SNe Ia have weaker *H*-band features, and the iron-peak material is responsible for the feature confined at lower velocities. Within the Chandrasekhar mass delayed-detonation scenario (Khokhlov 1991; Yamaoka et al. 1992), these correlations are expected because the strength and width of the *H*-band features are indicators of the amount of ^{56}Ni (Wheeler et al. 1998; Höflich et al. 2002). On the other hand, for explosion scenarios that produce a spread of explosion masses such as dynamical mergers (Iben & Tutukov 1984; Webbink 1984), or in the case of strong mixing, the correlations are expected to be weak.

The *H*-band break ratio measurements greatly simplify the analysis of the complex profile shape and time evolution of the *H*-band feature. In Fig. 15, we plot the time series of the *H*-band feature of four SNe Ia for comparison. SN 2011fe shows the *H*-band break forming at approximately three days past maximum and rapidly growing in strength. The characteristic double-peaked profile, formed by Fe II/Co II/Ni II, is typical of a normal SN Ia. iPTF13ebh and SN 2011iv are both low-luminosity, fast-declining objects in the transitional category, but the profile evolution of their *H*-band features is subtly different. At 1−2 weeks past maximum, the local minimum near 1.65 μm is more pronounced in SN 2011iv than in iPTF13ebh. The lack of a local minimum near 1.65 μm is a characteristic of the subluminous model presented by Höflich et al. (2002). By ~18 days past maximum, the *H*-band breaks for both iPTF13ebh and SN 2011iv have shifted redward in wavelength because of the decreasing size of the emission region at late times. The latest spectra shown in Fig. 15 for iPTF13ebh, SNe 1999by, and 2011iv share very similar profile shapes, with the appearance of a strong Fe II/Co II feature near 1.5 μm, which is usually weak in normal-bright SNe Ia. SN 1999by evolved to this profile shape approximately two weeks earlier than iPTF13ebh and SN 2011iv.

Increasing the central density causes a larger portion of material to undergo electron capture during deflagration and produces increasing amounts of stable ^{58}Ni (Höflich 2006). Using the time evolution of the detailed profile shape of the *H*-band complex, it is possible to isolate features produced by stable and unstable isotopes of iron-group elements and extract their mass ratio. This will be a subject of future studies with a larger data set.

5.4. Magnesium velocity

Magnesium is a product of explosive carbon burning, and not oxygen burning. This makes magnesium lines very sensitive to the location of the inner edge of carbon burning in velocity space (Wheeler et al. 1998; Marion et al. 2001, 2009; Höflich et al. 2002). The strong and isolated NIR Mg II $\lambda1.0927$ μm line is ideal for such a measurement. With early NIR spectroscopy of SN 2011fe, Hsiao et al. (2013) showed that the Mg II velocity declines rapidly and flattens between −10 to 10 days past maximum. The flattened Mg II velocity appears to be ubiquitous among normal SNe Ia. This means that it is possible to use a single snapshot NIR spectrum between −10 to 10 days past maximum to derive a characteristic minimum velocity for the given object.

We used the same PCA model of the Mg II profile as was presented in Hsiao et al. (2013) and the same fitting procedure using the nonlinear least-squares fitting program of Markwardt (2009) to determine the Mg II velocities and the uncertainties for iPTF13ebh and SN 2014J. These data points were added to Fig. 8 of Hsiao et al. (2013) and are presented in Fig. 16. The high-cadence observations of SN 2014J yielded a remarkably flat Mg II velocity, similar to that of SN 2011fe. The
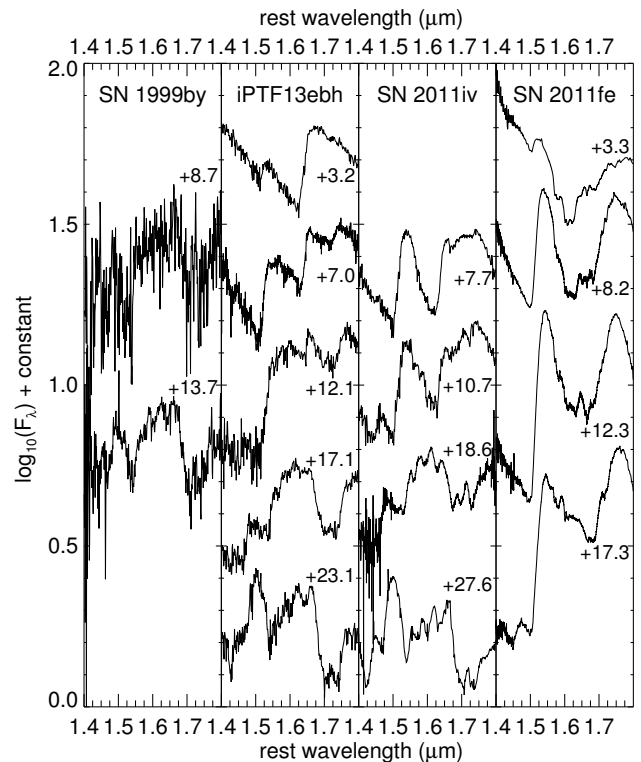
Fig. 15. Comparison of the *H*-band iron-peak feature between four SNe Ia. The phase with respect to *B*-band maximum is labeled for each spectrum.

Mg II velocity of SN 2014J is moderately high compared to other SNe Ia. Note that the Gaussian fitting method of Folatelli et al. (2013) gives systematic differences in velocities of ~300 km s^{-1}. This illustrates the importance of using a consistent technique within a comparison sample.

At early phase, the Mg II velocity of iPTF13ebh shows a rapid decline similar to SN 2011fe. In fact, because of the short rise time of iPTF13ebh, the rapidly declining portions of iPTF13ebh and SN 2011fe would line up if Fig. 16 was plotted in terms of explosion date. However, while the velocity evolution of SN 2011fe flattens to reveal the base of the carbon burning layer, the Mg II velocity of iPTF13ebh continues to decline. The Mg II line never reaches a minimum velocity while visible, indicating a deeper carbon burning layer than normal SNe Ia. In this respect, iPTF13ebh is similar to SN 1999by.

6. Transitional supernovae

The term "91bg-like", in the strictest sense, refers to spectroscopically peculiar SNe Ia that exhibit strong Ti II features in their maximum-light optical spectra, like SNe 1991bg (Filippenko et al. 1992; Branch et al. 1993; Leibundgut et al. 1993) and 1999by (Garnavich et al. 2004). These objects are found to be subluminous, have exceptionally fast-declining light curves, and are thought to originate from old population progenitors (Howell 2001). Subsequent studies revealed an apparent bimodality among fast-declining events when their NIR photometric properties are examined (e.g., Krisciunas et al. 2009; Folatelli et al. 2010; Phillips 2012). Events whose primary NIR maxima peak after the *B*-band maximum are subluminous in their absolute magnitudes in all bands compared to normal SNe Ia, even after taking the width-luminosity relation into account. These
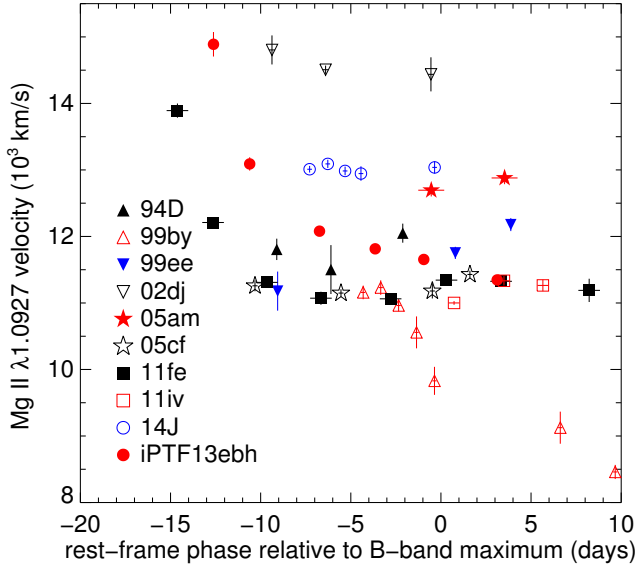
Fig. 16. Time evolution of the Mg II $\lambda1.0972\,\mu$m velocity. Various symbols represent different objects as noted in the plot. Blue, black, and red symbols represent SNe Ia with optical light-curve decline rates in the range $\Delta m_{15}(B) < 1.0$, $1.0 < \Delta m_{15}(B) < 1.6$, $\Delta m_{15}(B) > 1.6$, respectively. The Mg II $\lambda1.0972\,\mu$m velocity of iPTF13ebh decreases monotonically, indicating a deeper-reaching carbon-burning layer than normal SNe Ia.

Table 8. Optical light-curve parameters and the presence of Ti II of notable transitional events.

Name	$\Delta m_{15}(B)$	s_{BV}	Ti II	Data
SN 1986G	1.62 ± 0.02	0.65 ± 0.05	91bg-like	a
SN 2003gs	1.79 ± 0.04	0.46 ± 0.03	91bg-like	b
SN 2003hv	1.48 ± 0.04	0.76 ± 0.07	No Ti II	c
SN 2004eo	1.42 ± 0.03	0.83 ± 0.03	No Ti II	CSP; d
SN 2005am	1.53 ± 0.02	0.75 ± 0.02	No Ti II	CSP; d
SN 2007on	1.89 ± 0.01	0.55 ± 0.02	No Ti II	CSP; e
SN 2009an	1.64 ± 0.04	0.86 ± 0.06	No Ti II	f
SN 2011iv	1.76 ± 0.02	0.63 ± 0.01	No Ti II	CSP; g
SN 2012ht	1.30 ± 0.04	0.86 ± 0.03	No Ti II	CSP
iPTF13ebh	1.79 ± 0.01	0.63 ± 0.02	No Ti II	CSP

Notes. The $\Delta m_{15}(B)$ and s_{BV} values are measured using the data from the quoted sources.

References. [a] Phillips et al. (1987); [b] Krisciunas et al. (2009); [c] Leloudas et al. (2009); [d] Contreras et al. (2010); [e] Stritzinger et al. (2011); [f] Sahu et al. (2013); [g] Gall et al. (in prep.).

subluminous supernovae also tend to lack or have very weak secondary NIR maxima. The terms "91bg-like" and "subluminous" are spectroscopic and photometric definitions, respectively. So far, all SNe Ia with late-peaking NIR maxima have been found to have the spectroscopic peculiarity of strong Ti II, although, not all SNe Ia with Ti II signatures have late-peaking NIR maxima, as we describe below.

When defining "transitional" events between the fastest-declining normal SN Ia population and the 91bg-like/subluminous events, we chose the timing of the NIR primary maximum rather than the presence of Ti II as the defining feature. A transitional event is then defined as a fast-declining SN Ia with its NIR (*iYJHK*) primary maximum peaking before its *B*-band maximum. The case of SN 1986G (Phillips et al. 1987) is the main driver behind this choice of definition. For SN 1986G, Ti II is present in its spectra, like SN 1991bg, but its NIR absolute magnitudes place it with the normal SN Ia group. It is "91bg-like" spectroscopically, but not "subluminous" photometrically. Its NIR maxima also peak before *B* maximum. In our definition, SN 1986G is categorized as transitional with the normal SNe Ia and not with the subluminous group. More recently, SN 2003gs is also categorized as transitional and shows strong Ti II (Krisciunas et al. 2009). We recall that 91bg-like and subluminous are, strictly speaking, not the same group. However, since our discussions have been focused on spectroscopic properties, and our only NIR spectroscopic reference in the 91bg-like and subluminous groups is SN 1999by, we use the two terms interchangeably.

From Fig. 2, the primary maxima in *iYJH* light curves of iPTF13ebh clearly peak before its *B* maximum. And, unlike SNe 1986G and 1991bg, iPTF13ebh shows no evidence of Ti II in its optical spectra (Sect. 5.1). This clearly is a transitional event and has one of the fastest light-curve decline rates in this class. For comparison, the decline rates of some of the more notable transitional events are listed in Table 8.

While the width-luminosity relation (Phillips 1993) holds well for a wide range of luminosities and $\Delta m_{15}(B)$, there is a notable break at $\Delta m_{15}(B) \gtrsim 1.6$, where SNe Ia very quickly become faint with increased $\Delta m_{15}(B)$. Possibly related to this, $\Delta m_{15}(B)$ fails to properly classify the fastest-declining objects. The reason for this is that the onset of the linear decline in the *B*-band light curve occurs earlier than 15 days for the fastest decliners (Folatelli et al. 2010; Burns et al. 2011). This leads to poorly behaved light-curve templates and a seeming bimodality in the photometric properties of SNe Ia with $\Delta m_{15}(B)$. Using $\Delta m_{15}(B)$ for transitional objects is therefore problematical. Burns et al. (2014) introduced a new decline-rate parameter, s_{BV}, in an attempt to improve the treatment of the fast-declining objects. When s_{BV} is used, the fastest-declining events appear less as a distinct population and more as a continuous tail end of normal SNe Ia.

In Fig. 17, the Swope *i*-band light curve of iPTF13ebh is plotted in comparison with the normal and 91bg-like fits, as described by González-Gaitán et al. (2014). The fits were made with the light-curve fitter SiFTO (Conley et al. 2008), but with two sets of light-curve templates for comparison: one of normal SNe Ia and the other constructed from 91bg-like objects. The fitter stretches the time axis to fit the iPTF13ebh data from all of the optical *uBVgri*-bands. The result shows poor fits in the *i*-band for both normal and 91bg-like templates. iPTF13ebh has an *i*-band light curve morphology that bridges the two classes, with transitional properties, such as the timing of the primary and secondary peaks and the size of the secondary peak.

Figure 17 also shows comparison SNooPy fits using $\Delta m_{15}(B)$ and s_{BV} templates. The fits also include all optical *uBVgri*-bands. Unlike SiFTO fits, SNooPy takes into account the changing shape of the light curves in the redder filter bands for supernovae with different peak luminosities. The $\Delta m_{15}(B)$ template fit yields an *i*-band light curve with a primary maximum that peaks too early and a secondary maximum that peaks too late, which is characteristic of a brighter supernova than the *i*-band light curve suggests and is much like the normal SiFTO fit described above. The s_{BV} template, on the other hand, provides an excellent fit to the observed light curve. The effect would be even more pronounced in the NIR *YJH*-bands. We chose the *i*-band light curve for illustration because it has a much better coverage than the NIR bands (Fig. 2).
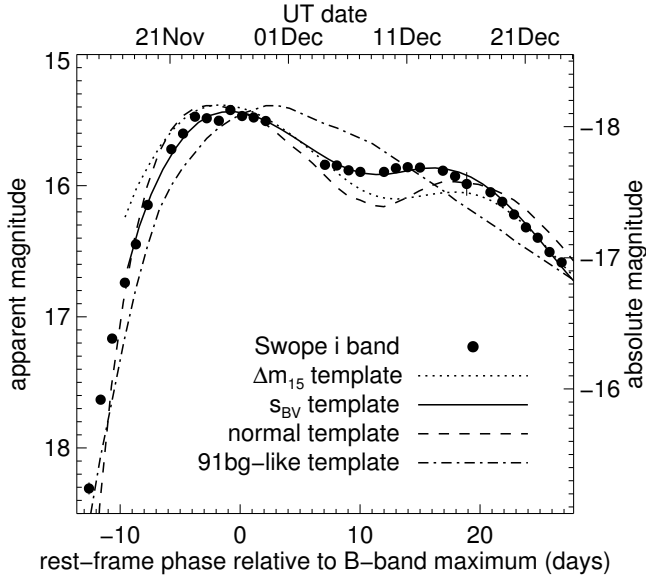
Fig. 17. Comparison of the Swope *i*-band light curve of iPTF13ebh to the `SNooPy` and `SiFTO` templates. The best `SNooPy` fits using $\Delta m_{15}(B)$ and s_{BV} *i*-band templates are plotted as dotted and solid curves, respectively. The best `SiFTO` fits with normal and 91bg-like templates are plotted as dashed and dot-dashed curves, respectively.

The photometric properties of iPTF13ebh place it with the normal SNe Ia, but many of its NIR spectroscopic properties, such as the strong C I, the profile shape of the *H*-band feature, and the Mg II velocity evolution, are similar to those of 91bg-like SN 1999by. `SNooPy` with the s_{BV} parameterization works well for iPTF13ebh and other transitional objects. This suggests a continuous range of properties across the transition. However, the s_{BV} parameter does not predict the presence of Ti II (nor does $\Delta m_{15}(B)$, see Table 8). It is unclear whether normal and subluminous/91bg-like belong in distinct groups or are objects with a common explosion mechanism and a continuous range of observed properties, but iPTF13ebh provides a connection between these subtypes.

7. Conclusions

iPTF13ebh is one of the fastest-declining and best-observed transitional objects between normal-bright and subluminous/91bg-like events. Overall, iPTF13ebh has properties that are distinct from either normal or subluminous classes. We summarize the main findings as follows:

1. The NIR *iYJH* light curves of iPTF13ebh peak before its *B* maximum, and its extinction-corrected absolute magnitudes obey the width-luminosity relation.
2. Several C I lines are detected in the early NIR spectra of iPTF13ebh. The C I $\lambda 1.0693$ μm line at 2.3 days past explosion (-12.8 days relative to *B* maximum) is the strongest ever observed in a SN Ia.
3. The profile of the C I $\lambda 1.0693$ μm line at first resembles that of SN 1999by, a subluminous/91bg-like object. However, while the strong C I line persists until maximum light in SN 1999by, the C I line of iPTF13ebh quickly weakens and takes on a profile similar to that of a normal SN Ia.
4. The NIR C I $\lambda 1.0693$ μm line of iPTF13ebh is much stronger than its optical C II $\lambda 0.6580$ μm line. This property is general

among SNe Ia with C I detections, and contradicts the prediction of stronger C II lines by Tanaka et al. (2008).
5. Unlike normal SNe Ia, iPTF13ebh shows flat C I velocity evolution, indicating that the base of the unburned layer is already reached at the earliest phases.
6. The *H*-band break ratio of iPTF13ebh fits well in the peak ratio versus $\Delta m_{15}(B)$ relation previously found by Hsiao et al. (2013). The strong correlation is consistent with the Chandrasekhar-mass delayed-detonation scenario, while the correlation is expected to be weak in dynamical mergers.
7. By late time, the profile shape of the *H*-band complex resembles that of SN 1999by. The composition and density of the inner core of iPTF13ebh is therefore similar to that of 91bg-like events.
8. Unlike in normal SNe Ia, the Mg II velocity of iPTF13ebh monotonically decreases with time, indicating a carbon burning layer that reaches deeper than normal SNe Ia. This behavior is similar to that of SN 1999by.
9. There is no evidence of a detached high-velocity component for the Ca II NIR triplet of iPTF13ebh as early as 3.2 days past explosion, providing a stringent constraint on when this high-velocity feature could have formed, if it ever existed.
10. iPTF13ebh has a substantial difference between the explosion times inferred from the early-time light curve and the velocity evolution of the Si II $\lambda 0.6355$ μm line, implying a long dark-phase of ~ 4 days.

The data set presented here is unique because the follow-up campaign began shortly after explosion and spanned a wide wavelength coverage from the UV to the NIR. iPTF13ebh is also the only transitional SN Ia with extensive NIR spectroscopic coverage. The photometric properties of iPTF13ebh suggest that it is at the fast-declining end of normal SNe Ia. The NIR spectra reveal many similarities to the 91bg-like SN 1999by, however. The rare glimpse of the NIR spectroscopic properties of a transitional event provides a connection between normal and the peculiar subluminous/91bg-like events, perhaps indicating a common explosion mechanism.

References

Albrecht, A., Bernstein, G., Cahn, R., et al. 2006, ArXiv e-prints [arXiv:astro-ph/0609591]

Amanullah, R., Goobar, A., Johansson, J., et al. 2014, ApJ, 788, L21

Benetti, S., Cappellaro, E., Mazzali, P. A., et al. 2005, ApJ, 623, 1011

Blondin, S., Matheson, T., Kirshner, R. P., et al. 2012, AJ, 143, 126

Boldt, L. N., Stritzinger, M. D., Burns, C., et al. 2014, PASP, 126, 324

Branch, D., Fisher, A., & Nugent, P. 1993, AJ, 106, 2383

Branch, D., Garnavich, P., Matheson, T., et al. 2003, AJ, 126, 1489

Branch, D., Baron, E., Hall, N., Melakayil, M., & Parrent, J. 2005, PASP, 117, 545

Branch, D., Dang, L. C., Hall, N., et al. 2006, PASP, 118, 560

Branch, D., Troxel, M. A., Jeffery, D. J., et al. 2007, PASP, 119, 709

Breeveld, A. A., Landsman, W., Holland, S. T., et al. 2011, AIP Conf Ser., 1358, 373

Brown, P. J., Dawson, K.S., de Pasquale, M., et al. 2012, ApJ, 753, 22

Brown, P. J., Breeveld, A. A., Holland, S., Kuin, P., & Pritchard, T. 2014a, Ap&SS, 301

Brown, P. J., Smitka, M. T., Wang, L., et al. 2014b, ArXiv e-prints [arXiv:1408.2381]

Burns, C. R., Stritzinger, M., Phillips, M. M., et al. 2011, AJ, 141, 19

Burns, C. R., Stritzinger, M., Phillips, M. M., et al. 2014, ApJ, 789, 32

Cao, Y., Hsiao, E. Y., Phillips, M. M., et al. 2013, ATel, 5580, 1

Childress, M. J., Filippenko, A. V., Ganeshalingam, M., & Schmidt, B. P. 2014, MNRAS, 437, 338

Conley, A., Howell, D. A., Howes, A., et al. 2006, AJ, 132, 1707

Conley, A., Sullivan, M., Hsiao, E. Y., et al. 2008, ApJ, 681, 482

Contreras, C., Hamuy, M., Phillips, M. M., et al. 2010, AJ, 139, 519

Cushing, M. C., Vacca, W. D., & Rayner, J. T. 2004, PASP, 116, 362

De, S., Baron, E., & Hauschildt, P. H. 2010, MNRAS, 401, 2081

de Vaucouleurs, G., de Vaucouleurs, A., Corwin, HG, Jr., et al. 1991, Third Reference Catalogue of Bright Galaxies (New York: Springer)

Dessart, L., Blondin, S., Hillier, D. J., & Khokhlov, A. 2014, MNRAS, 441, 532

Diamond, T., Hoeflich, P., & Gerardy, C. L. 2014, ApJ, submitted [arXiv:1410.6759]

Dressler, A., Bigelow, B., Hare, T., et al. 2011, PASP, 123, 288

Elias, J. H., Vukobratovich, D., Andrew, J. R., et al. 1998, Proc. SPIE, 3354, 555

Faber, S. M., Phillips, A. C., Kibrick, R. I., et al. 2003, Proc. SPIE, 4841, 1657

Filippenko, A. V. 1982, PASP, 94, 715

Filippenko, A. V., Richmond, M. W., Branch. D., et al. 1992, AJ, 104, 1543

Firth, R. E., Sullivan, M., Gal-Yam, A., et al. 2015, MNRAS, 446, 3895

Folatelli, G., Phillips, M. M., Burns, Christopher R., et al. 2010, AJ, 139, 120

Folatelli, G., Morrell, N., Phillips, M. M., et al. 2012, ApJ, 745, 74

Folatelli, G., Phillips, M. M., Morrell, N., et al. 2013, ApJ, 773, 53

Foley, R. J., Kromer, M., Howie M. G., et al. 2012, ApJ, 753, L5

Foley, R. J., Fox, O. D., McCully, C., et al. 2014, MNRAS, 443, 2887

Friesen, B., Baron, E., Wisniewski, J. P., et al. 2014, ApJ, 792, 120

Gamezo, V. N., Khokhlov, A. M., Oran, E. S., Chtchelkanova, A. Y., & Rosenberg, R. O. 2003, Science, 299, 77

Gamezo, V. N., Khokhlov, A. M., & Oran, E. S. 2004, Phys. Rev. Lett., 92, 211102

Garavini, G., Folatelli, G., Goobar, A., et al. 2004, AJ, 128, 387

Garnavich, P. M., Bonanos, A. Z., Krisciunas, K., et al. 2004, ApJ, 613, 1120

Gehrels, N., Chincarini, G., Giommi, P., et al. 2004, ApJ, 611, 1005

Gerardy, C. L., Höflich, P., Fesen, R. A., et al. 2004, ApJ, 607, 391

González-Gaitán, S., Hsiao, E. Y., Pignata, G., et al. 2014, ApJ, 795, 142

González-Martín, O., Rodràguez-Espinosa, J. M., Díaz-Santos, T., et al. 2013, A&A, 553, A35

Goobar, A., & Leibundgut, B. 2011, Ann. Rev. Nucl. Part. Sci., 61, 251

Goobar, A., Johansson, J., Amanullah, R., et al. 2014, ApJ, 784, L12

Goobar, A., Garnavich, P. M., Kessler, R., et al. 2015, ApJ, 799, 106

Hayden, B. T., Garnavich, P. M., Kessler, R., et al. 2010, ApJ, 712, 350

Höflich, P. 1990, A&A, 229, 191

Höflich, P. 2002, ArXiv e-prints [arXiv:astro-ph/0207103]

Höflich, P. 2006, Nucl. Phys. A, 777, 579

Höflich, P. 2009, AIP. Conf. Ser., 1171, 161

Höflich, P., Khokhlov, A. M., & Wheeler, J. C. 1995, ApJ, 444, 831

Höflich, P., Khokhlov, A., Wheeler, J. C., et al. 1996, ApJ, 472, L81

Höflich, P., Gerardy, C. L., Fesen, R. A., & Sakai, S. 2002, ApJ, 568, 791

Höflich, P., Gerardy, C. L., Nomoto, K., et al. 2004, ApJ, 617, 1258

Horne, K. 1986, PASP, 98, 609

Howell, D. A. 2001, ApJ, 554, L193

Howell, D. A., Sullivan, M., Nugent, P. E., et al. 2006, Nature, 443, 308

Hoyle, F., & Fowler, W. A. 1960, ApJ, 132, 565

Hsiao, E. Y. 2009, Ph.D. Thesis, University of Victoria

Hsiao, E. Y., Marion, G. H., Phillips, M. M., et al. 2013, ApJ, 766, 72

Iben, I., Jr., & Tutukov, A. V. 1984, ApJS, 54, 335

Kasen, D., Röpke, F. K., & Woosley, S. E. 2009, Nature, 460, 869

Kelson, D. D. 2003, PASP, 115, 688

Khokhlov, A. M. 1991, A&A, 245, 114

Kirshner, R. P., Willner, S. P., Becklin, E. E., Neugebauer, G., & Oke, J. B. 1973, ApJ, 180, L97

Kozma, C., Fransson, C., Hillebrandt, W., et al. 2005, A&A, 437, 983

Krisciunas, K., Marion, G. H., Suntzeff, N. B., et al. 2009, AJ, 138, 1584

Landolt, A. U. 1992, AJ, 104, 340

Leibundgut, B., Kirshner, R. P., Phillips, M. M., et al. 1993, AJ, 105, 301

Leloudas, G., Stritzinger, M. D., Sollerman, J., et al. 2009, A&A, 505, 265

Maguire, K., Sullivan, M., & Nugent, P. 2013, ATel, 5584, 1

Maguire, K., Sullivan, M., Pan, Y.-C., et al. 2014, MNRAS, 444, 3258

Marion, G. H., Höflich, P., & Wheeler, J. C. 2001, Rev. Mex. Astron. Astrof. Conf. Ser., 10, 190

Marion, G. H., Höflich, P., Wheeler, J. C., et al. 2006, ApJ, 645, 1392

Marion, G. H., Höflich, P., Gerardy, C. L., et al. 2009, AJ, 138, 727

Marion, G. H., Sand, D. J., Hsiao, E. Y., et al. 2015, ApJ, 798, 39

Markwardt, C. B. 2009, in ADASS XVIII, 18th Conf. Series, eds. D. Bohlender, D. Durand, & P. Dowler, 411, 251

Matheson, T., Kirshner, R. P., Challis, P., et al. 2008, AJ, 135, 1598

Mazzali, P. A., Benetti, S., Altavilla, G., et al. 2005, ApJ, 623, L37

Mazzali, P. A., Sauer, D. N., Pastorello, A., Benetti, S., & Hillebrandt, W. 2008, MNRAS, 386, 1897

Milne, P. A., Brown, P. J., Roming, P. W. A., Bufano, F., & Gehrels, N. 2013, ApJ, 779, 23

Motohara, K., Maeda, K., Gerardy, C. L., et al. 2006, ApJ, 652, L101

Mould, J. R., Huchra, J. P., Freedman, W. L., et al. 2000, ApJ, 529, 786

Nugent, P., Phillips, M., Baron, E., Branch, D., & Hauschildt, P. 1995, ApJ, 455, L147

Nugent, P. E., Sullivan, M., Cenko, S. B., et al. 2011, Nature, 480, 344

Oke, J. B., & Gunn, J. E. 1982, PASP, 94, 586

Oke, J. B., Cohen, J. G., Carr, M., et al. 1995, PASP, 107, 375

Parrent, J. T., Thomas, R. C., Fesen, R. A., et al. 2011, ApJ, 732, 30

Parrent, J. T., Howell, D. A., Friesen, B., et al. 2012, ApJ, 752, L26

Pastorello, A., Mazzali, P. A., Pignata, G., et al. 2007, MNRAS, 377, 1531

Penney, R., & Höflich, P. 2014, ApJ, 795, 84

Perlmutter, S., Aldering, G., Goldhaber, G., et al. 1999, ApJ, 517, 565

Persson, S. E., Murphy, D. C., Krzeminski, W., Roth, M., & Rieke, M. J. 1998, AJ, 116, 2475

Phillips, M. M. 1993, ApJ, 413, L105

Phillips, M. M. 2012, PASA, 29, 434

Phillips, M. M., Phillips, A. C., Heathcote, S. R., et al. 1987, PASP, 99, 592

Phillips, M. M., Lira, P., Suntzeff, N. B., et al. 1999, AJ, 118, 1766

Piro, A. L., & Nakar, E. 2013, ApJ, 769, 67

Piro, A. L., & Nakar, E. 2014, ApJ, 784, 85

Röpke, F. K., Hillebrandt, W., Schmidt, W., et al. 2007, ApJ, 668, 1132

Rahmer, G., Smith, R., Velur, V., et al. 2008, Proc. SPIE, 7014

Rasmussen, C. E., & Williams, C. K. I. 2006, Gaussian Processes For Machine Learning (The MIT Press)

Rayner, J. T., Toomey, D. W., Onaka, P. M. et al. 2003, PASP, 115, 362

Rheault, J.-P., DePoy, D. L., Behm, T. W., et al. 2010, Proc. SPIE, 7735, 773564

Rheault, J.-P., Mondrik, N. P., DePoy, D. L., Marshall, J. L., & Suntzeff, N. B. 2014, Proc. SPIE, 9147, 91475

Riess, A. G., Filippenko, A. V., Challis, P., et al. 1998, AJ, 116, 1009

Roming, P. W. A., Kennedy, T. E., Mason, K. O., et al. 2005, Space Sci. Rev., 120, 95

Sahu, D. K., Anupama, G. C., & Anto, P. 2013, MNRAS, 430, 869

Scalzo, R. A., Aldering, G., Antilogus, P., et al. 2010, ApJ, 713, 1073

Silverman, J. M., & Filippenko, A. V. 2012, MNRAS, 425, 1917

Silverman, J. M., Ganeshalingam, M., Li, W., et al. 2011, MNRAS, 410, 585

Simcoe, R. A., Burgasser, A. J., Schechter, P. L., et al. 2013, PASP, 125, 270

Smith, J. A., Tucker, D. L., Kent, S., et al. 2002, AJ, 123, 2121

Stritzinger, M. D., Phillips, M. M., Boldt, L. N., et al. 2011, AJ, 142, 156

Stritzinger, M. D., Valenti, S., Hoeflich, P., et al. 2015, A&A, 573, A2

Sullivan, M., Conley, A., Howell, D. A., et al. 2010, MNRAS, 406, 782

Tanaka, M., Mazzali, P. A., Benetti, S., et al. 2008, ApJ, 677, 448

Taubenberger, S., Benetti, S., Childress, M., et al. 2011, MNRAS, 412, 2735

Telesco, C. M., Höflich, P., Li, D., et al. 2015, ApJ, 798, 93

Thomas, R. C., Aldering, G., Antilogus, P., et al. 2007, ApJ, 654, L53

Thomas, R. C., Aldering, G., Antilogus, P., et al. 2011a, ApJ, 743, 27

Thomas, R. C., Nugent, P. E., & Meza, J. C. 2011b, PASP, 123, 237

Vacca, W. D., Cushing, M. C., & Rayner, J. T. 2003, PASP, 115, 389
Wang, X., Filippenko, A. V., Ganeshalingam, M., et al. 2009, ApJ, 699, L139
Webbink, R. F. 1984, ApJ, 277, 355
Wheeler, J. C., Höflich, P., Harkness, R. P., & Spyromilio, J. 1998, ApJ, 496, 908
Woods, D. F., Geller, M. J., & Barton, E. J. 2006, AJ, 132, 197
Wyrzykowski, L., Campbell, H. C., Koposov, S., et al. 2014, ATel, 5926, 1
Yamanaka, M., Maeda, K., Kawabata, M., et al. 2014, ApJ, 782, L35
Yamaoka, H., Nomoto, K., Shigeyama, T., & Thielemann, F.-K. 1992, ApJ, 393, L55
Yaron, O., & Gal-Yam, A. 2012, PASP, 124, 668
Zheng, W., Shivvers, I., Filippenko, A. V., et al. 2014, ApJ, 783, L24

[1] Department of Physics and Astronomy, Aarhus University, Ny Munkegade 120, 8000 Aarhus C, Denmark
e-mail: hsiao@phys.au.dk

[2] Carnegie Observatories, Las Campanas Observatory, Colina El Pino, Casilla 601, Chile

[3] Carnegie Observatories, 813 Santa Barbara St, Pasadena, CA 91101, USA

[4] Florida State University, Tallahassee, FL 32306, USA

[5] Physics Department, Texas Tech University, Lubbock, TX 79409, USA

[6] University of Texas at Austin, 1 University Station C1400, Austin, TX 78712-0259, USA

[7] Harvard-Smithsonian Center for Astrophysics, 60 Garden Street, Cambridge, MA 02138, USA

[8] Millennium Institute of Astrophysics, Casilla 36-D, Santiago, Chile

[9] Departamento de Astronomía, Universidad de Chile, Casilla 36-D, Santiago, Chile

[10] Gemini Observatory, Northern Operations Center, Hilo, HI 96720, USA

[11] Instituto de Astrofísica de La Plata (IALP), CCT-CONICET-UNLP, Paseo del Bosque S/N, B1900FWA La Plata, Argentina

[12] Kavli Institute for the Physics and Mathematics of the Universe (WPI), The University of Tokyo, Kashiwa, Chiba 277-8583, Japan

[13] Department of Physics, Bishop's University, Sherbrooke, Quebec, J1M 1Z7, Canada

[14] Dark Cosmology Centre, Niels Bohr Institute, University of Copenhagen, Juliane Maries vej 30, 2100 Copenhagen, Denmark

[15] The Oskar Klein Centre, Physics Department, Stockholm University, Albanova University Center, 106 91 Stockholm, Sweden

[16] Indian Institute of Astrophysics, Koramangala, Bangalore 560034, India

[17] Las Cumbres Observatory Global Telescope Network, Goleta, CA 93117, USA

[18] Physics Department, University of California, Santa Barbara, CA 93106, USA

[19] Astronomy and Astrophysics Division, Physical Research Laboratory, Navrangapura, Ahmedabad − 380009 Gujarat, India

[20] Department of Astronomy, University of California, Berkeley, CA 94720-3411, USA

[21] Department of Physics and Astronomy, Texas A&M University, College Station, TX 77843, USA

[22] Cahill Center for Astrophysics, California Institute of Technology, Pasadena, CA 91125, USA

[23] Computational Cosmology Center, Computational Research Division, Lawrence Berkeley National Laboratory, 1 Cyclotron Road MS 50B-4206, Berkeley, CA 94611, USA

[24] European Southern Observatory for Astronomical Research in the Southern Hemisphere (ESO), Karl-Schwarzschild-Str. 2, 85748 Garching b. München, Germany

[25] University of Arizona, Steward Observatory, 933 North Cherry Avenue, Tucson, AZ 85719, USA

[26] Department of Particle Physics and Astrophysics, Weizmann Institute of Science, 76100 Rehovot, Israel

[27] Instituto de Astrofísica, Facultad de Física, Pontificia Universidad Católica de Chile, Chile

[28] School of Physics and Astronomy, University of Southampton, Southampton SO17 1BJ, UK

[29] Spitzer Science Center, MS 314-6, California Institute of Technology, Pasadena, CA 91125, USA

[30] Space & Remote Sensing, MS B244, Los Alamos National Laboratory, Los Alamos, NM 87545, USA